

Effects of Residual Stress and Equivalent Bending Stiffness on the Dimensional Stability of the Thin-Walled Parts

Hanjun Gao

Beijing University of Aeronautics and Astronautics

Xin Li

Beijing University of Aeronautics and Astronautics

Qiong Wu (✉ wuqiong@buaa.edu.cn)

Beijing University of Aeronautics and Astronautics <https://orcid.org/0000-0003-2460-8558>

Minghui Lin

Beijing University of Aeronautics and Astronautics

Yidu Zhang

Beijing University of Aeronautics and Astronautics

Research Article

Keywords: residual stress, equivalent bending stiffness, dimensional stability, machining deformation, topology optimization

Posted Date: May 17th, 2021

DOI: <https://doi.org/10.21203/rs.3.rs-511993/v1>

License:  This work is licensed under a Creative Commons Attribution 4.0 International License.

[Read Full License](#)

Version of Record: A version of this preprint was published at The International Journal of Advanced Manufacturing Technology on January 13th, 2022. See the published version at <https://doi.org/10.1007/s00170-021-08252-3>.

Effects of residual stress and equivalent bending stiffness on the dimensional stability of the thin-walled parts

Hanjun Gao^{a,b,c}, Xin Li^a, Qiong Wu^{a*}, Minghui Lin^a, Yidu Zhang^a

- a. State Key Laboratory of Virtual Reality Technology and Systems, School of Mechanical Engineering and Automation, Beihang University, Beijing, 100191, PR China;
- b. Anhui HengLi Additive Manufacturing Technology Co. LTD., Wuhu, 241200, PR China;
- c. Anhui Chungu 3D Printing Institute of Intelligent Equipment and Industrial Technology, Wuhu, 241220, PR China;

Abstract:

The monolithic thin-walled parts are widely used in the aeronautic and astronautic field because of its excellent mechanical performance and light weight, but the thin-walled parts are vulnerable to the machining deformation due to its low stiffness and high material removal rate. According to the relative basic theory, the stiffness and internal residual stress of the part are the critical factors affecting the dimensional stability. In this work, the influences of equivalent bending stiffness and residual stress on the dimensional stability of thin-walled parts are studied. Nine typical thin-walled parts in three groups with two materials (7075 aluminum alloy for A1~A3 and B1~B3, and Ti6Al4V titanium alloy for B4~B6) are machined and treated with different processes. Topology optimization technique is used to optimize the structure of parts to enhance the bending stiffness. Corresponding finite element method (FEM) simulations are carried out to further investigate the generation mechanism. The deformations in 312 hours after machining are measured using coordinate measuring machine, and the deformation changes of the parts are obtained and analyzed. Finally, based on topological optimization and

stress relief technology, a machining deformation control method for the monolithic thin-walled parts is proposed. Results show that the maximum and average deformations of thin-walled are evidently decreased using the proposed method.

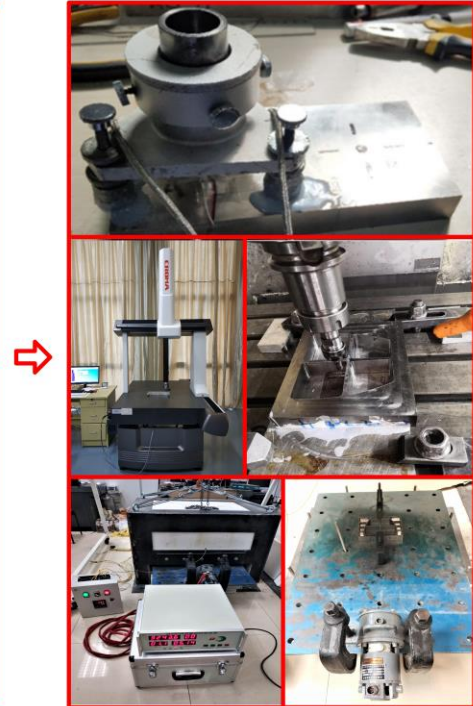
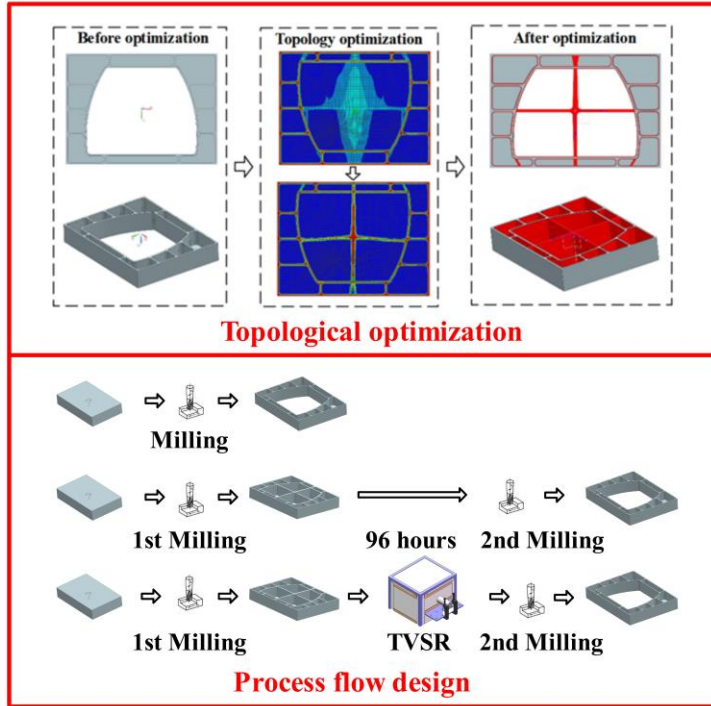
Keywords: residual stress; equivalent bending stiffness; dimensional stability; machining deformation; topology optimization;

Corresponding author: Wu Qiong, wuqiong@buaa.edu.cn

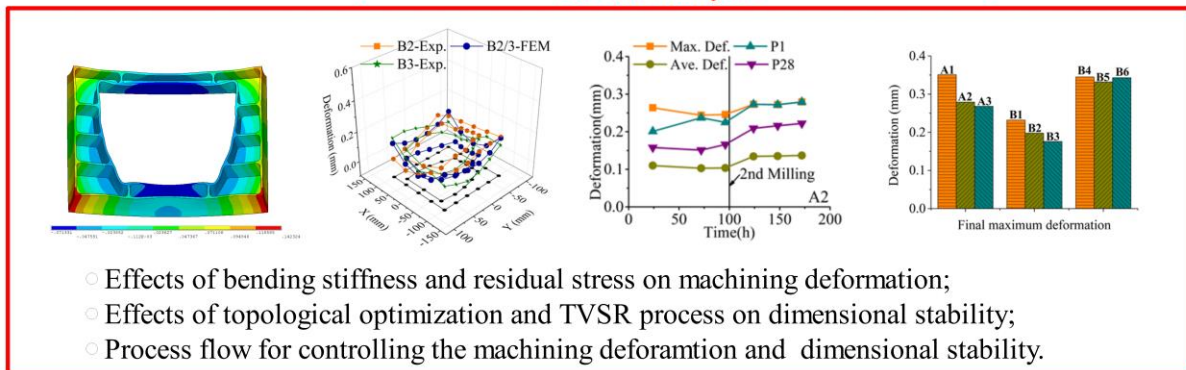
Graphical Abstract

Deformation control method research

Experimental verification



Results analysis



1. Introduction

The monolithic thin-walled parts have been widely used in the aerospace products because of its high strength and low weight. However, due to the high material removal rate, low stiffness and complex structure, the machining accuracy is difficult to control. Therefore, the problem of machining deformation and dimensional stability of the monolithic thin-walled parts has always been the focus of scholars' researches.

The machining is a highly nonlinear thermal-structural coupling process, which is affected by a lot of factors. Tang et al. [1] pointed out that the initial residual stress, machining induced residual stress, clamping force, cutting force, as well as cutting heat are the main factors of machining deformation. Fu et al. [2] mentioned that the release and rebalance of residual stress is the main factor of machining deformation, and they proposed a new method to calculate the initial residual. Huang et al. [3, 4] explored the impact of the initial residual stress of blank, the machining induced residual stress and the coupling of these two factors on the deformation. It was found that the initial residual stress of three-frame beam is the main factor of deformation, while for the aluminum alloy plate, the machining induced residual stress is the major factor. On the basis of a large number of literature research, Li and Wang [5] systematically summarized the influence of residual stress on machining deformation as well as the control methods for aviation aluminum alloy, which can offer a good guidance for researchers in related fields.

Scholars have conducted a series of research to study the machining process of the monolithic

thin-walled parts, and then to predict and control the machining deformation. Ren et al. [6] regarded the multi pocket structure as a combination of Kirchhoff plates, combined the vibration model with the dynamic cutting model, and established the control equation which fully considers the dynamic characteristics of the thin-walled milling process. For the pre-bent plate, considering the coupling effect of bending stress and the machining induced residual stress, Li et al. [7] analyzed the mechanism of deformation through theoretical analysis and numerical simulation, and corresponding experiments were carried out to validate the correctness of deformation mechanism.

Finite element (FE) simulation plays an important role in machining deformation prediction. Considering the influence of deformation caused by the cutting force and multi-point contact structure dynamics in the contact area, Sun and Jiang [8] proposed a modeling method of dynamic milling system. Wang and Si [9] established a flexible iterative simulation model to predict deformation in the more complicated five-axis flank milling process. Similarly, Wang et al. [10] constructed an analytical model for frame parts that can predict deformation caused by residual stress and verified its accuracy through experiments.

In addition, plenty of achievements have been made in the control of machining deformation. Ma et al. [11] put forward a method to make the machining deformation uniform by planning the cutting amount. Kou et al. [12] used auxiliary support to balance the axial cutting force and control the deformation in milling process. To solve the process adjustment of the deformed workpiece in multiple processes, Hao et al. [13] proposed a geometry modeling method, which

can be used to accurately reconstruct the deformation workpiece model, so as to conduct more accurate analysis in the next process.

Increasing the stiffness of part can reduce its deformation effectively, and topology optimization is a common method to increase the part's stiffness. Topology optimization refers to finding the optimal structure configuration for specific conditions in a given design domain. Through comparison with other various topology optimization methods, both Sigmund et al. [14] and Deaton et al. [15] considered that solid isotropic material with poverty model is the most popular and successful method due to its simplicity of the concept and numerical implementation. Topology optimization is often applied with 3D printing technology. Vanek et al. [16] proposed an optimization approach which can successfully complete the established support function with less support structure. Langelaar, M. [17] constructed a system which can generate fully self-supporting structures in the additive manufacturing process using the topology optimization technology. Liu, J. et al. [18] systematically analyzed the development trends of topology optimization for 3D printing technology, providing some feasible suggestions for relevant researchers.

Except for the field of 3D printing, Zhu et al. [19] and Wang et al. [20] comprehensively summarized the broad application prospects of topology optimization in the field of aerospace and medicine, respectively. In aviation industry, topology optimization can be used for optimal design of materials, components and systems. While in the field of medicine, it can be used to obtain the best internal structure of porous implant which can meet the requirements of multi-

function and simulate human bone. Besides, Liu, J. and Y. Ma [21] investigated the manufacturing-oriented topology optimization methods, and pointed out some potential development directions of topology optimization in manufacturing, such as concurrent optimization of the related position path. From above it can be seen that topology optimization has been widely used in engineering practice successfully and can effectively solve the problem.

Reducing the internal residual stress of thin-walled parts is another approach to control the deformation. Dong et al. [22] pointed out that if there is still large residual stress in the part after machining, some degree of deformation will inevitably occur in the process of residual stress release. Therefore, some stress relief processes can be taken to homogenize the internal residual stress of parts, and the commonly used technologies include thermal stress relief (TSR), vibratory stress relief (VSR), thermal and vibratory stress relief (TVSR), ultrasonic vibration, mechanical deformation method, etc.

Gu et al. [23] established a unified ultrasonic vibration plasticity framework and revealed the mechanism of the ultrasonic stress relief, which has an important significance in ultrasonic stress homogenization. Gao et al. [24] investigated the effect of VSR on residual stress and fatigue life of Ti6Al4V part. Yan et al. [25] used creep model considering temperature effect to predict residual stress release during post weld heat treatment (PWHT) and carried out experimental verification. The research results showed that there is a critical temperature (740 K), about which the residual stresses of Ti6Al4V start to decrease mathematically during PWHT, and the strain increment caused by creep dominated the residual stress relief. Chen et al. [26]

took 2219 aluminum alloy welding specimen as research object, studied and compared the effects of TSR, VSR, and TVSR. Results showed that TSR reduced the peak residual stress more effectively, and the elimination effect of TVSR is more ideal under the resonance frequency and medium temperature. Wu et al. [27] applied the method of TVSR to SiCP/Al composites material and expanded the scope of its application.

In terms of mechanical deformation method, Koc, M et al. [28] compared the effects of two different cold working methods of compression and stretching on residual stress relief, and the results showed that both processes could reduce the residual stresses more than 90% while the former was more economical. Ran et al. [29] and Gong et al. [30] adopted the cold rolling and roll-bending process respectively to eliminated the residual stress of aluminum alloy generated during the quenching process. Although the means to eliminate residual stress are various, their principles are similar, that is use certain methods to input energy into the aging piece, so that the stress state inside the part is more uniform.

It can be known that there are two effective ways to reduce the machining deformation of monolithic thin-walled structure: increasing its bending stiffness and reducing its residual stress. The residual stress is the driving force of deformation and the bending stiffness is the resistance one. To study the influence of equivalent bending stiffness and TVSR on the dimensional stability of thin-walled parts, nine typical parts in three groups with two materials (7075 aluminum alloy for A1~A3 and B1~B3, and Ti6Al4V titanium alloy for B4~B6) are machined and treated with different processes. Topology optimization technique is used to optimize the

structure of parts to enhance the bending stiffness. Corresponding FEM simulations are carried out to further investigate the generation mechanism. The deformations in hundreds of hours after machining are measured using coordinate measuring machine, and the deformation changes of the parts are obtained and analyzed. Finally, a machining deformation control method for thin-walled parts based on topological optimization and stress relief process is summarized and proposed.

2. Theory

2.1 Equivalent bending stiffness

The expression of plate's bending stiffness is shown as follows [31],

$$D = \frac{Eh^3}{12(1-\mu^2)} \quad (1)$$

where D is the bending stiffness, h is the thickness of the plate, E and μ is the elastic modulus and Poisson's ratio of the material respectively.

The equivalent thickness and equivalent bending stiffness of frame parts can be calculated by static analysis using FEM. Thus, the analytical model of plate part can be extended to the general thin-walled parts, and this process is shown in **Fig.S1**. The maximum deformation in X and Y directions (dis_x and dis_y) are obtained respectively under uniform load q_x and q_y . The thin-walled part is equivalent to a cantilever beam and its maximum deformation can be expressed as the Eq. (2) if a vertical force F is applied to the cantilever end,

$$wl = \frac{4F \cdot len^3}{E \cdot bl \cdot hl^3}, \quad (2)$$

where wl is the maximum deformation, and len , bl , hl are the length, width and thickness of the cantilever beam respectively.

Therefore, the equivalent thickness and equivalent bending stiffness of frame parts in X and Y directions could be expressed as follows,

$$h_{eqvx} = \left(\frac{4F_x L^3}{dis_x \cdot E \cdot W} \right)^{\frac{1}{3}}, \quad (3)$$

$$h_{eqvy} = \left(\frac{4F_y W^3}{dis_y \cdot E \cdot L} \right)^{\frac{1}{3}}, \quad (4)$$

$$D_{eqvx} = \frac{E \cdot h_{eqvx}^3}{12(1 - \mu^2)}, \quad (5)$$

$$D_{eqvy} = \frac{E \cdot h_{eqvy}^3}{12(1 - \mu^2)}, \quad (6)$$

where L and W are the length and width of the workpiece respectively, $F_x = q_x \cdot W$, $F_y = q_y \cdot L$.

2.2 Machining deformation calculation

As shown in **Fig.1**, the initial and machining induced residual stress will lead to the inevitable deformation. According to the results of Zhang et al. [32], the bending deformation caused by the unbalance of residual stress in a certain direction can be equivalent to the bending deformation caused by applying uniform moment to the two opposite edges. Therefore, when calculating the deformation of the plate workpiece with bi-directional initial residual stress, it can be equivalent to apply uniform bending moment on both opposite sides. Through theoretical derivation, the bottom deflection function of thin-walled frame part is obtained,

$$w_i(x, y) = \frac{1}{2} \left(\frac{1}{R_{x,i}} x^2 + \frac{1}{R_{y,i}} y^2 \right), \left(-\frac{L}{2} \leq x \leq \frac{L}{2}, -\frac{W}{2} \leq y \leq \frac{W}{2} \right), \quad (7)$$

where $R_{x,i}$ and $R_{y,i}$ are the curvature radius of workpiece in X and Y directions after the layer i

is been stripped, and their expressions are as following,

$$\frac{1}{R_{x,i-1}} - \frac{1}{R_{x,i}} = \frac{6f_i(\sigma_{x,i-1,1} \cdot t \cdot h_i - \mu\sigma_{y,i-1,1} \cdot t \cdot h_i + \sigma_{xma,i} P_{x,i} t - \mu\sigma_{yma,i} P_{y,i} t)}{Eh_{eqvx,i}^3}, \quad (8)$$

$$\frac{1}{R_{y,i-1}} - \frac{1}{R_{y,i}} = \frac{6f_i(\sigma_{y,i-1,1} \cdot t \cdot h_i - \mu\sigma_{x,i-1,1} \cdot t \cdot h_i + \sigma_{yma,i} P_{y,i} t - \mu\sigma_{xma,i} P_{x,i} t)}{Eh_{eqvy,i}^3}. \quad (9)$$

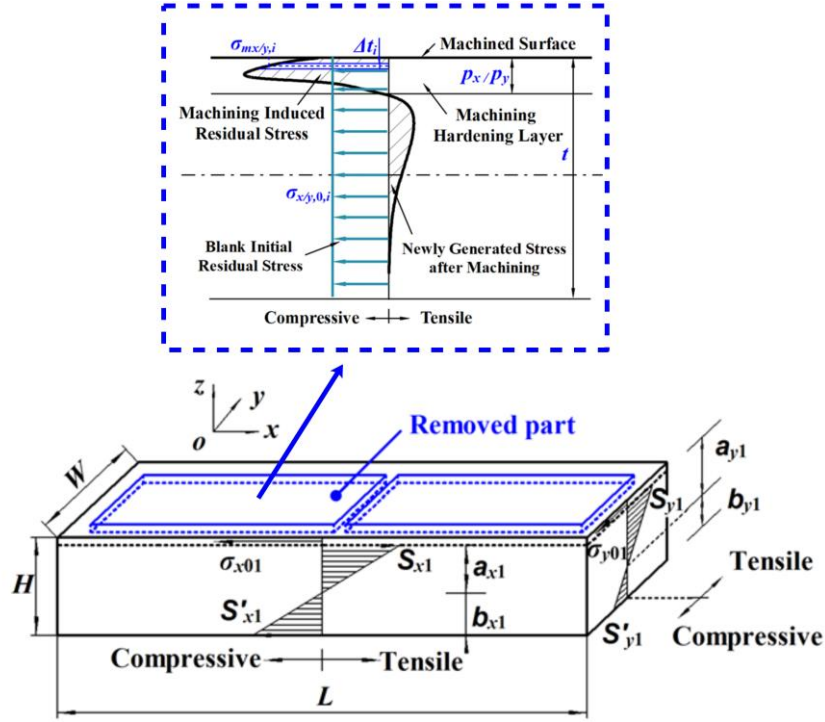


Fig.1 Deformation caused by blank initial and machining induced residual stress [33]

Among them, $h_{eqvx,i}$ and $h_{eqvy,i}$ are the equivalent thickness of the remaining workpiece in X and Y directions after the layer i is been removed, f_i is the volume fraction of removed material in layer i , h_i is the total thickness of the workpiece before stripping layer i , t is the stripped thickness of each layer, E and μ are the elastic model and Poisson's ratio respectively.

It can be seen that equivalent thickness is the pivotal parameter to deduce the deformation from the Eq. (7) ~ (9). Moreover, Eq. (5) ~ (6) show that the equivalent stiffness is proportional

to the cubic of equivalent thickness when the material is fixed. Therefore, increasing the thin-walled part's equivalent stiffness can effectively reduce its machining deformation.

3. Specimen design

The release and redistribution of residual stress will lead to the deformation. With the same stress distribution, increasing the equivalent stiffness of the workpiece can effectively reduce its deformation. In this study, some stiffening ribs are designed in specific positions through topology optimization, which can significantly improve the equivalent stiffness of the workpiece with the similar material removal rate.

3.1 Topology optimization

Topology optimization based on FEA is an effective method of structural optimization design. A topological optimization problem with exponential approximation can be defined in Eq. (10) ~ (13):

$$\min_X : c(X) = U^T K U = \sum_{e=1}^N (x_e)^p u_e^T k_0 u_e, \quad (10)$$

$$K U = F, \quad (11)$$

$$\text{subject to: } \frac{V(X)}{V_0} = f, \quad (12)$$

$$0 < X \min \leq x \leq 1, \quad (13)$$

where U and F represent the global displacement vector and force vector respectively, and K represents the overall stiffness matrix of the structure. K , U and F satisfy the Eq. (11). X is the design variable that represents the density of the material at each location. The objective function makes the deformation energy of the structure minimum under external load. Eq. (12)

~ (13) represent two constraints: the volume fraction f of the optimized volume in the design domain, and the optimized density which between X_{min} and 1.

The size and shape of original thin-walled parts are shown in **Fig.2**. Then, the simulation of topological optimization is carried out using the OptiStruct module of Hypermesh software to improve the bending stiffness.

As is presented in Section 2.2, the initial and machining induced residual stress are the primary factors on the machining deformation of thin-walled parts. The load formed by residual stress release could be equivalent to uniform bending moment of two opposite sides, so the static analysis is selected to simulate the release of residual stress. Uniform loads are applied in length and width direction respectively, and the fixed constraints are applied in the center line (**Fig.S2** and **Fig.S3**). The obtained displacement is taken as the constraint variables of topology optimization, and the volume fraction of the optimization region is taken as the optimization objective. Thus, the minimum volume fraction of the optimization region that can also satisfy the displacement constraint is obtained, and the morphology of the stiffening ribs are outputted as the optimization results.

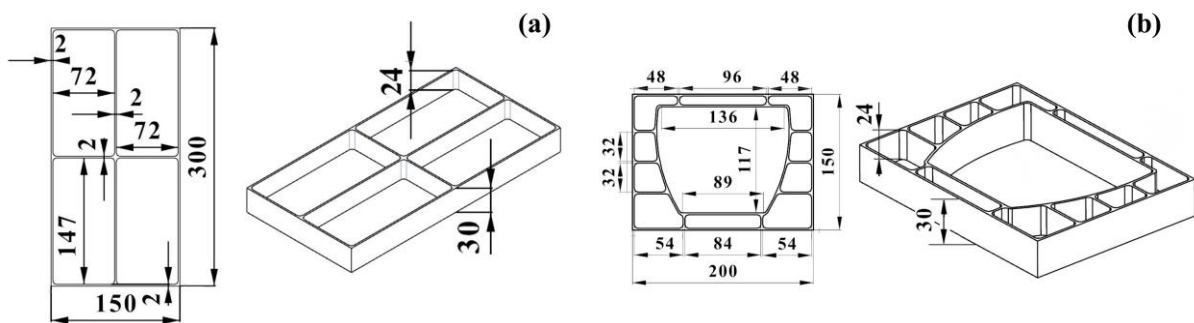


Fig.2 Size and shape sketch of two kinds thin wall parts(a)A-type part, and (b)B-type part

3.2 Determination of specimen

The optimal A-type and B-type parts are calculated after 49 and 123 iterations in Hyperworks software, and their topology optimization results are shown in **Fig.3** and **Fig.4**. It shows that the topological morphology has initially appeared when the number of iterations reaches about 50%. The subsequent iteration calculations further modify and refine the basic morphology. Results show that a thick stiffener is generated parallel to the central axis of the long side direction, while some relatively short and thin stiffeners are generated at the local position to strengthen its stiffness.

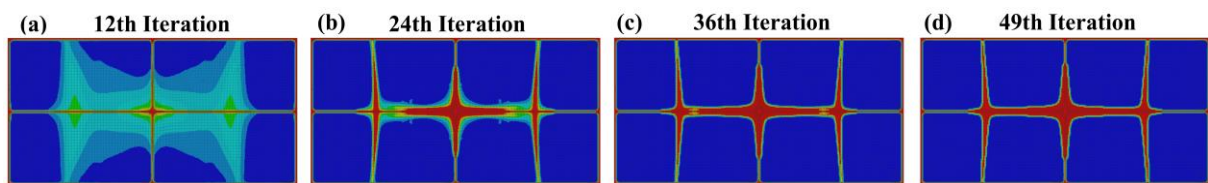


Fig.3 Topology optimization results of A-type parts after (a) 12th iteration, (b) 24th iteration, (c) 36th iteration, and (d) 49th iteration

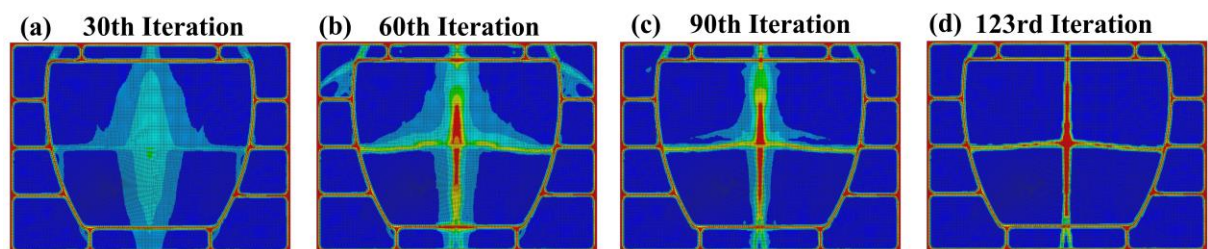


Fig.4 Topology optimization results of B-type parts after (a) 30th iteration, (b) 60th iteration, (c) 90th iteration, and (d) 123rd iteration

Based on the topological optimization results and considering the machinability at the same time, some stiffening ribs are added to improve the bending stiffness during machining process (**Fig.5**). Then, the original model and optimized model are imported into ANSYS to calculate their equivalent bending stiffness, respectively. The comparison results are shown in **Tab. 1**. It

shows that the equivalent bending stiffness after topology optimization is significantly improved. Meanwhile, due to the addition of stiffeners, the volume of retained materials increases, resulting in a slight reduction of material removal rate. Results show that the D_{eqvx} (equivalent bending stiffness in X direction) of Type A and B increases by 63.23% and 89.34% respectively; D_{eqvy} (equivalent bending stiffness in Y direction) increases by 427.64% and 174.59% respectively, and the material removal ratio reduces by 8.54% and 7.71% respectively.

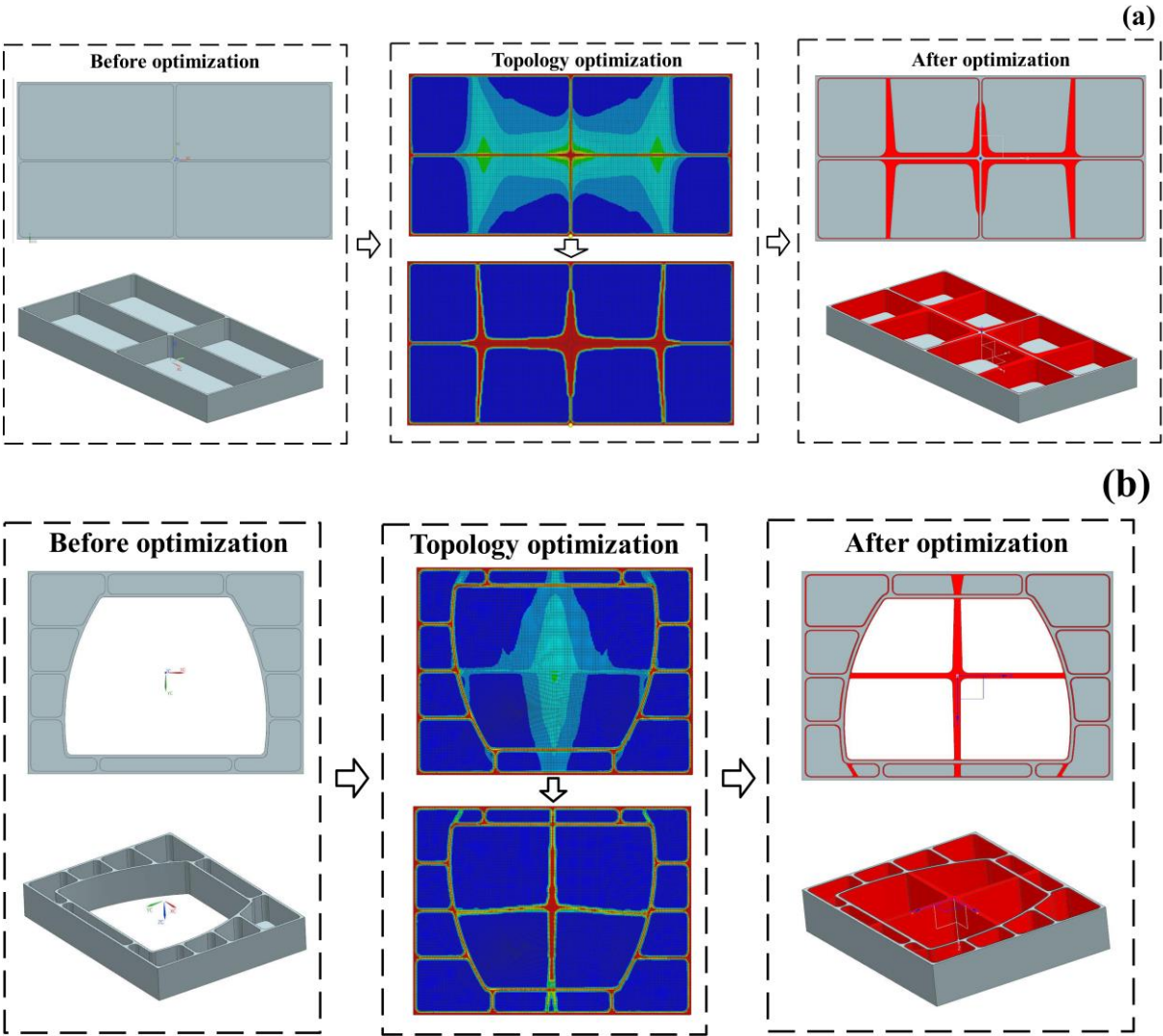


Fig.5 Design results of (a) Type A, (b) Type B

Tab. 1 Comparison of equivalent bending stiffness before and after topology optimization (material removal rate equals material removal volume / blank volume)

Performance comparison	Type A		Percentage	Type B		Percentage
	Before optimization	After optimization		Before optimization	After optimization	
D_{eqvx} (N·mm)	2.01×10^7	3.28×10^7	+63.23%	4.23×10^7	8.01×10^7	+89.34%
D_{eqvy} (N·mm)	9.27×10^6	4.89×10^7	+427.64%	5.27×10^6	1.45×10^7	+174.59%
Mass (kg)	75.17%	66.63%	-8.54%	82.47%	74.75%	-7.71%

4. Simulations and experiments

4.1 Initial residual stress measurement tests

The initial stress of specimen blank should be tested before machining simulations and experiments. One 7075 aluminium alloy (**Fig.6b**) and one Ti6Al4V specimen (**Fig.6e**), whose sizes are both $300 \times 150 \times 30$ mm, are used for residual stress measurement tests. The blind-hole and ring-core method are combined to measure the residual stress along the depth direction. RS-200 micro-measurement device that produced by Vishay Co., Ltd. (USA) is used for blind-hole tests, which can measure the residual stress within 0-2mm depth under the surface (**Fig.6a** and **Fig.6d**). And RKV-18 device that produced by Laubinger + Rickmann GmbH & Co. KG (Germen) is used for the ring-core tests, which can measure the residual stress within 2-4mm depth under the surface (**Fig.6c** and **Fig.6f**).

Thus, the average values within 0-2mm and 2-4 mm depth under the surface are measured by the blind-hole and ring-core method, respectively. Subsequently, the material within 4mm under the surface is removed by a YCM-CNC-116B machining center (produced by Yongjin machinery Co., Ltd, China) with $\phi 125$ mm milling tools, and the combination of the two methods are utilized again to obtain the residual stress under new surface using layer-removed

method. As a result, residual stresses within 0-16 mm depth can be measured, and the measured value is corrected by the modified formula of layer-removed method.

The residual stress profiles of 7075 aluminium alloy and Ti6Al4V specimens are presented in Fig. 7. The stress values of 16-32mm and 0-16mm are symmetrical.

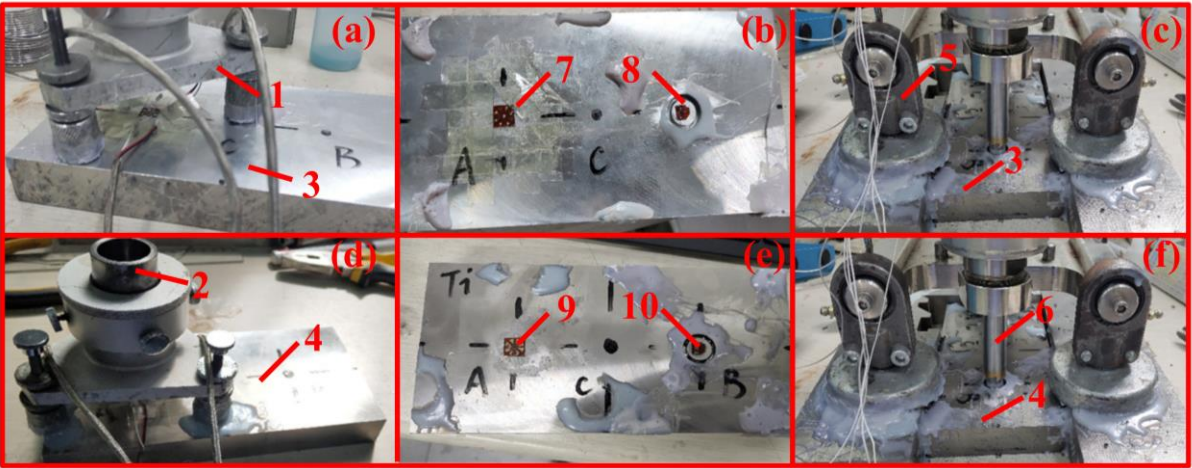


Fig.6 Residual stress measurement tests: (a) blind-hole method for 7075 aluminium alloy, (b) 7075 aluminium alloy specimen with measurement point, (c) ring-core method for 7075 aluminium alloy, (d) blind-hole method for Ti6Al4V, (e) Ti6Al4V specimen with measurement point, and (f) ring-core method for Ti6Al4V (1-Fixture of RS200, 2-Spinde of RS200, 3-7075 aluminium alloy specimen, 4- Ti6Al4V specimen, 5-Fixture of RKV-18, 6-Spindle of RKV-18, 7-Blind-hole test point for 7075 aluminium alloy, 8- Ring-core test point for 7075 aluminium alloy, 9-Blind-hole test point for Ti6Al4V, and 10-Ring-core test point for Ti6Al4V)

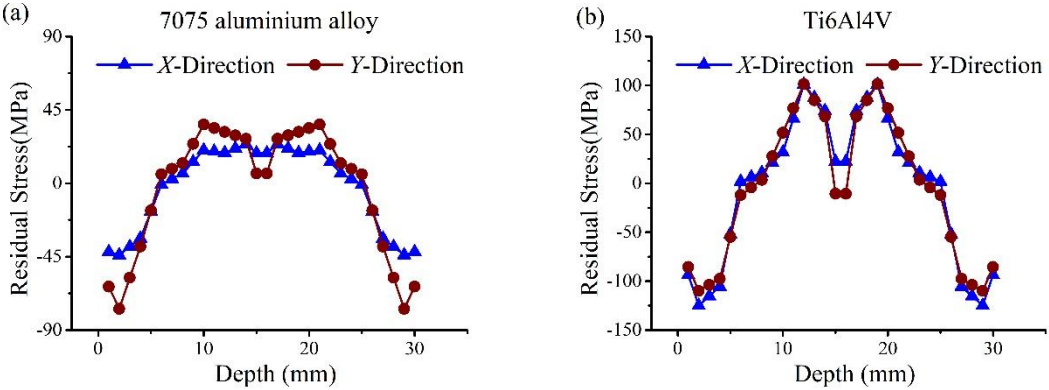


Fig. 7 Residual stress profiles of (a) 7075 aluminium alloy and (b) Ti6Al4V

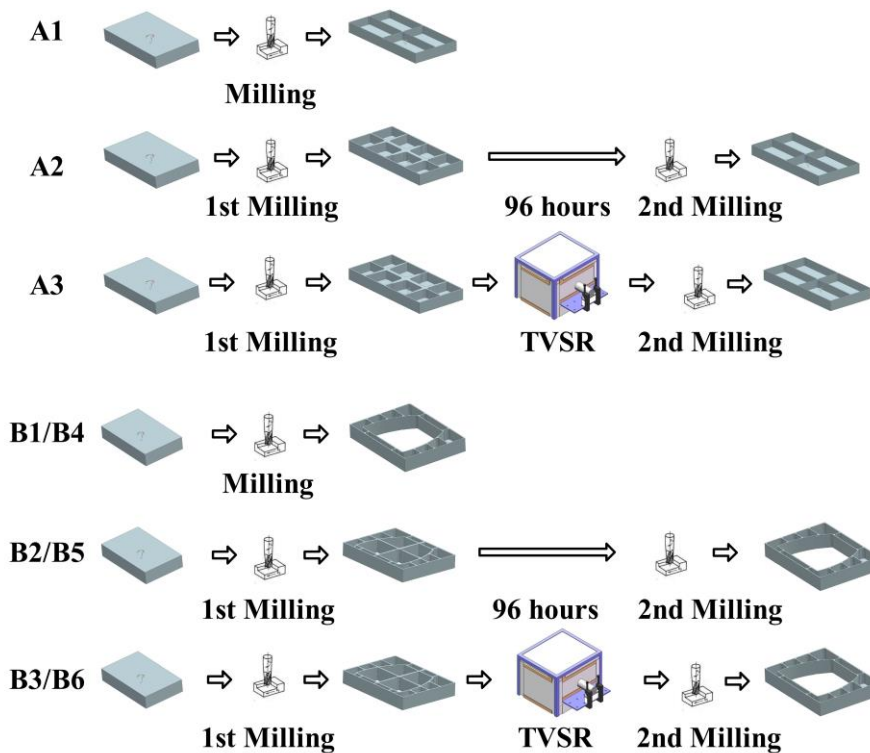
4.2 Experiments

Based on the model before and after topology optimization, different machining and stress relief processes are applied to 7075 aluminum alloy and Ti6Al4V titanium alloy, respectively (**Fig. 8**). There are two kinds of parts with different shapes, named A1~A3 and B1~B6, respectively. Type A parts are divided into one group, whose material is 7075 aluminum alloy, while type B parts are divided into two groups, whose material are 7075 aluminum alloy (B1~B3) and Ti6Al4V titanium alloy (B4~B6), respectively. Each group contains three parts, corresponding to three different processes:

Process 1 (A1, B1, B4): the blank is machined to the final shape directly;

Process 2 (A2, B2, B5): the stiffening ribs are reserved in the 1st machining, and after 96 h natural aging treatment (waiting for 96 hours in the unsteady room temperature), the reserved stiffeners are removed in the 2nd machining;

Process 3 (A3, B3, B6): the stiffening ribs are reserved in the 1st machining, and TVSR is conducted to further reduce the residual stress. Finally, the reserved stiffeners are removed in the 2nd machining.



A1, A1, A3, B1, B2 and B3 are 7075 aluminium alloy, and B4, B5 and B6 are Ti6Al4V.

Fig. 8 Process flows of the specimens

Among them, the TVSR mentioned in Process 3 is a new residual stress control method. The traditional TSR has a significant effect on global stress relief yet requires high energy consumption. VSR is green and environmentally friendly, but it is mainly used to eliminate the stress value of key parts. In some cases, the overall stress relief effect is not so significant. The method of TVSR integrates the advantages of TSR and VSR. At the same time of TSR, it provides vibration excitation to the working platform, which can significantly reduce the internal residual stress of workpiece and achieve a good stress homogenization effect. The mechanism of TVSR is as follows: the yield strength of material will be reduced at high temperature. Under the action of vibration excitation, the residual stress of workpiece will be superimposed with the vibration dynamic stress, and plastic strain occurs in parts exceeding the

yield strength of material, which will release the residual stress.

The experimental equipment of TVSR is developed and built by the author's own team. As shown in **Fig. 9**, the equipment is composed by heating system and vibration system. When working, the workpiece is clamped on the vibration platform, and the vibration exciter stimulates the platform to drive the overall vibration of workpiece. At the same time, the thermal aging furnace covers the vibration platform, and the aging temperature of heating furnace is adjusted by the temperature controller. The workpiece releases its internal residual stress under the coupling effect of vibration and heat.

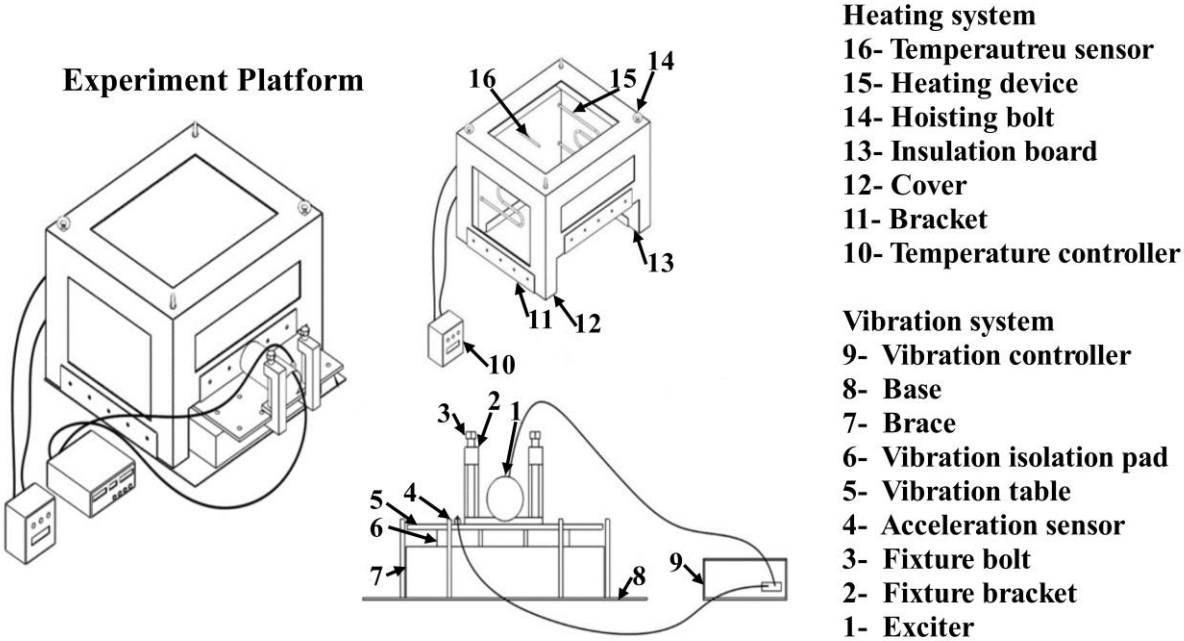


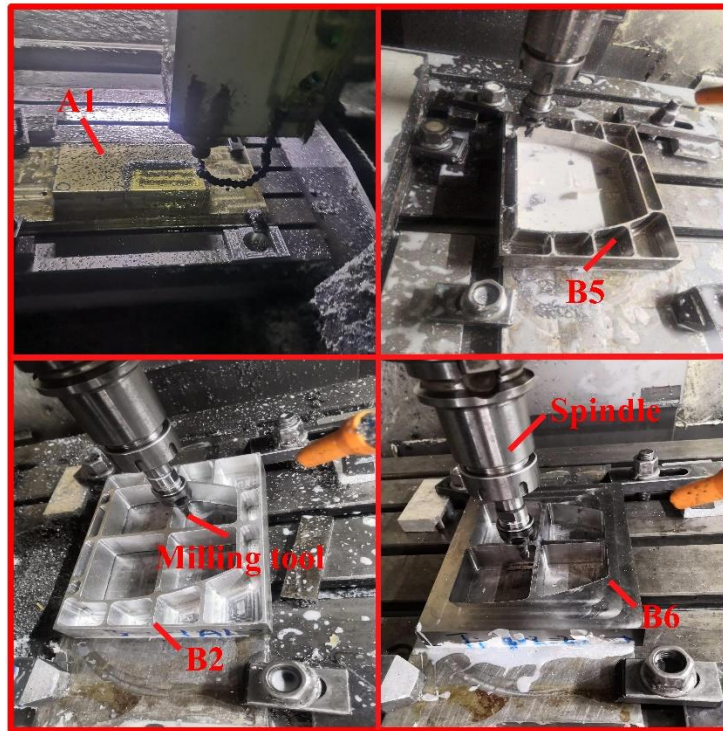
Fig. 9 the schematic diagram of structural composition of TVSR [34]

Taking A3 and B3 for example to introduce the process flow in **Fig. 8**, their bottom surface deformations are measured at 24 hours after machining, and the TVSR is carried out. The

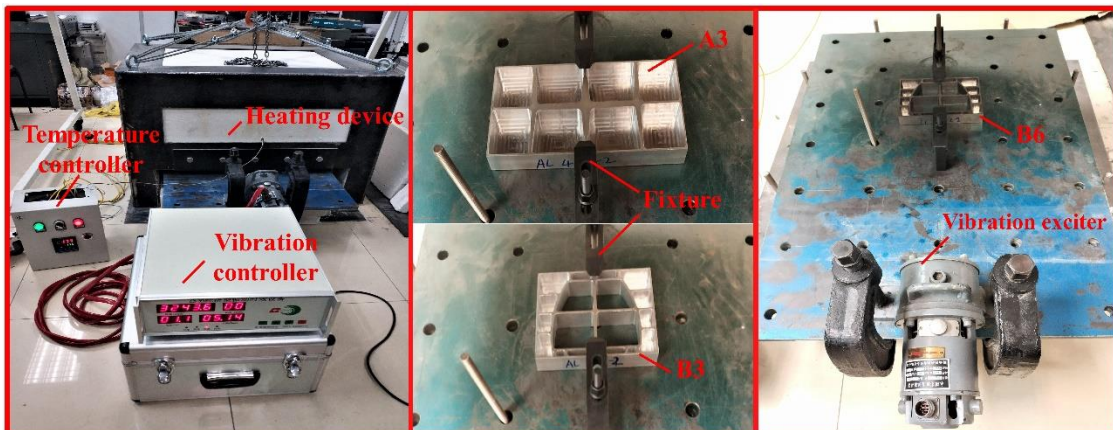
holding temperatures of titanium alloy and aluminum alloy of TVSR are 280°C and 175° C, respectively. According to the measured resonance frequency, the vibration frequency of A3 and B3 are set as 60.5hz and 60.3hz respectively, and the corresponding rotational speed of eccentric motor is 3630 r/min and 3618 r/min respectively. The process flow of TVSR for aluminum alloy workpiece (A3, B3) is as follows:

- 1) 0-30min: heat the workpiece from 25 °C to 175 °C evenly;
- 2) 30-60min: keep the temperature within 175 °C ± 2 °C for 0.5h;
- 3) 60-65min: vibrate with resonance frequency for 5min at 175 °C;
- 4) 65-95min: keep the temperature within 175 °C ± 2 °C for 0.5h;
- 5) 95-100min: vibrate with resonance frequency for 5min at 175 °C;
- 6) 100-340min: Stop heating, cool with the furnace for 4 hours, and air cool to room temperature after removing the fixture.

Particularly, compared with the aluminum alloy specimen, the titanium alloy one has different vibration frequencies as well as the holding temperature and time. The titanium alloy keeps the holding temperature within 280 °C ± 2 °C for 60min and the total time is 370 min. The NC machining and TVSR process of A-type and B-type parts are shown in **Fig.10**.



(a)



(b)

Fig.10 NC machining and TVSR processing: (a) Part of the B-type parts on-site processing, and (b) TVSR of A-type and B-type parts

In order to explore the influences of topological structure and TVSR on the dimensional accuracy and stability, deformation measurements are carried out for many times in hundreds of hours. The number and time of deformation measurement are shown in **Tab. 2**. M1 and M2 in the table represent the 1st and 2nd milling, respectively. **Fig.S4** is the location and distribution

of the measuring points of each workpiece, and **Fig.11** presents the measurement device.

Tab. 2 the number and time of deformation measurement of A1~A3 and B1~B6 (M1 and M2 represent the first and second processing respectively)

No.	A1	A2	A3	B1	B2	B3	B4	B5	B6
1	M1_24h	M1_24h	M1_24h	M1_24h	M1_24h	M1_24h	M1_24h	M1_24h	M1_24h
2	M1_72h	M1_72h	M1_72h	M1_72h	M1_72h	M1_72h	M1_72h	M1_72h	M1_72h
3	M1_96h	M1_96h	M1_96h	M1_96h	M1_96h	M1_96h	M1_96h	M1_96h	M1_96h
4	M1_120h	M2_24h	M2_24h	M1_216h	M2_24h	M2_24h	M1_240h	M2_24h	M2_24h
5	M1_312h	M2_48h	M2_48h	M1_312h	M2_48h	M2_48h	M1_312h	M2_48h	M2_48h
6		M2_72h	M2_72h	/	M2_72h	M2_72h	/	M2_72h	M2_72h

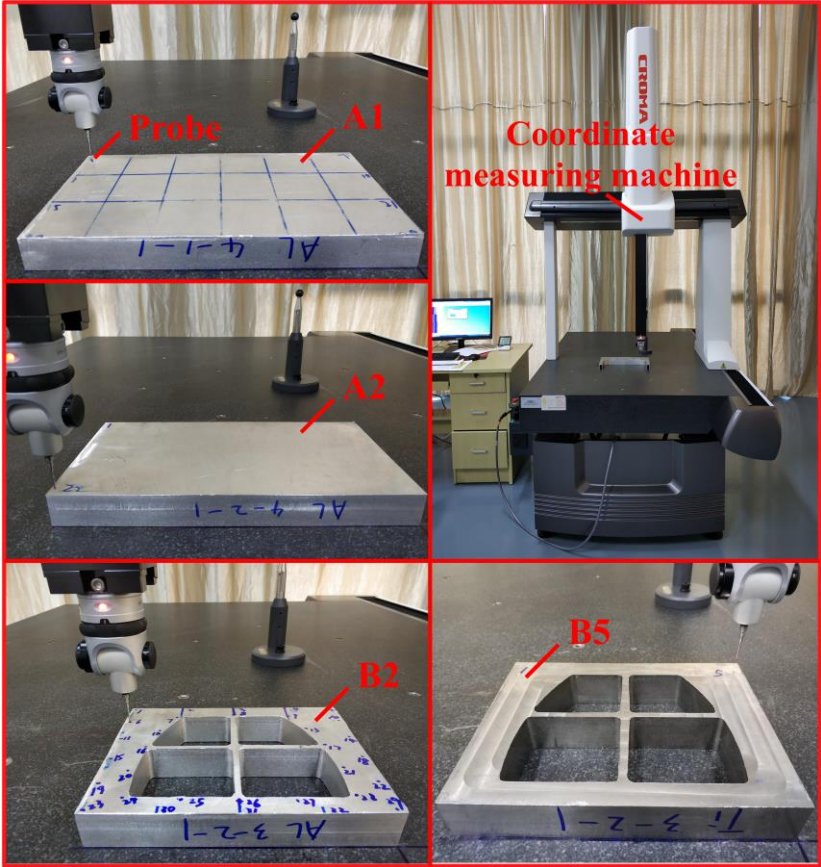


Fig.11 Deformation measurement experiment

4.3 Machining simulations

To further study the influences of equivalent bending stiffness and residual stress on the machining deformation and the dimensional stability, FE models of machining process are

established by the combination of AdvantEdge and ANSYS software. The nonlinear thermal-structure coupling model of milling process is built using AdvantEdge to calculate the machining induced residual stress, the milling force as well as the temperature at local positions. The milling parameters of 7075 aluminium alloy and Ti6Al4V are the same as the experiments.

The milling process model of the whole workpiece is built in ANSYS software. The solid 186 element with 20 nodes is selected, and the geometry model with machining and non-machining area are imported into ANSYS. Then, the geometric model is discretized into finite element model through meshing. (Fig.12). The initial and the machining induced residual stress, as well as other results calculated by AdvantEdge are assigned to the layer of FE model, and the material removed process is simulated with birth and death element method. Thus, the deformation and stress during milling process can be calculated after the material is removed from the blank layer by layer.

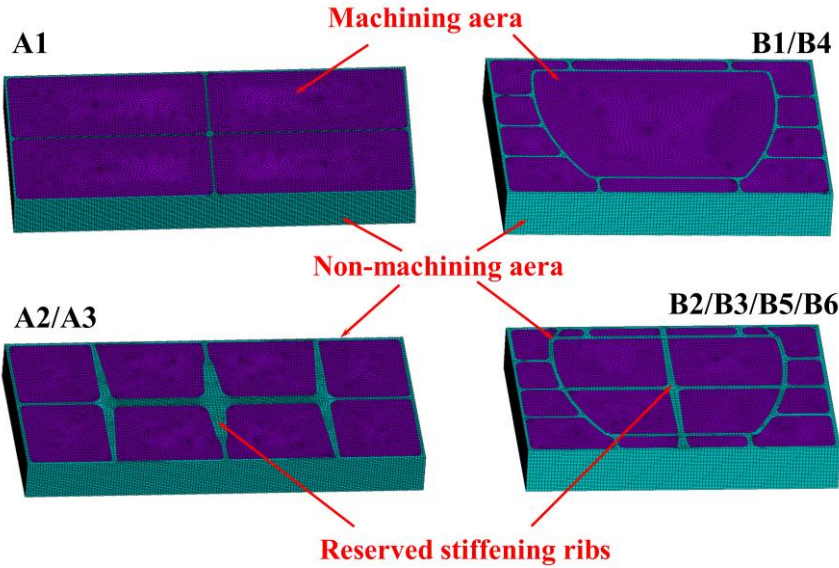


Fig.12 FE models of specimens

5. Results and discussions

5.1 Comparison of FEM and experiment results

Fig.S5 presents the machining induced residual stresses calculated by AdvantEdge software. Stress results on three quartering points of the machined surface are extracted and summarized, and the average values of the three points are taken as the simulation results. It shows that a compressive stress layer is formed on the machined surface, and some tensile stress exists in the subsurface layer. For 7075 aluminum alloy, the maximum compressive stress, average stress and stress layer depth in the X direction are -108 MPa, -51 MPa and 0.14 mm, respectively, and those in Y direction are -141MPa, -94 MPa and 0.04 mm, respectively. For Ti6Al4V, those in X direction are -238 MPa, -120 MPa and 0.12 mm, respectively, and those in Y direction are -258 MPa, -121 MPa, 0.09 mm, respectively.

The deformations after the 1st milling caused by the blank initial and machining induced residual stresses of the specimens are demonstrated in **Fig.13**. Results shows that the bottom surface of the parts is approximately an elliptical surface, and the peak deformation occurs at four corners, which is in accordance with the theory in Section 2.

Fig.14 presents the FEM and experimental deformation results of the measuring points on the bottom surface. It can be seen the deformation distribution of FEM agrees well with experiment. Because A2 and A3, B2 and B3, and B5 and B6 have the same shape after 1st milling, the calculated results between two parts are the same, while the measured results are different. Therefore, the calculated results are compared to the average measured value of two

parts (A2/A3, B2/B3, and B5/B6).

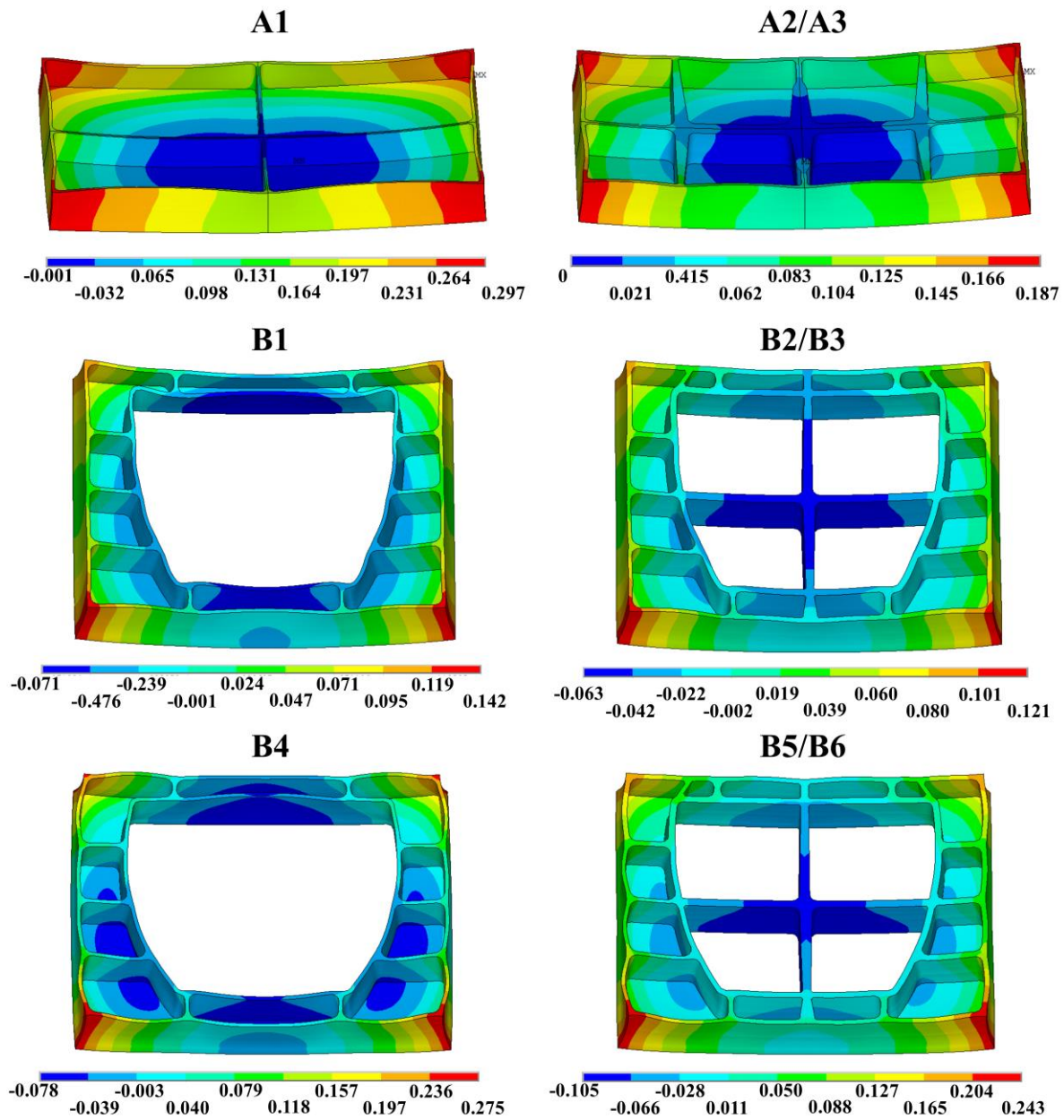


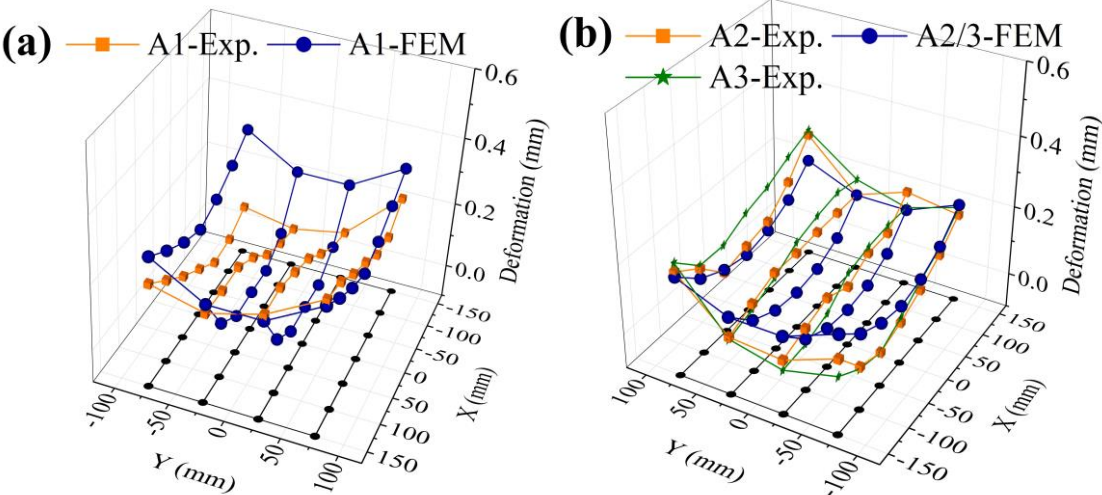
Fig.13 FEM deformation contours after 1st milling

The calculated peak deformation of A1 and A2/A3 are 0.297 and 0.187mm, and the measured results are 0.315 and 0.271mm; the calculated average value of 28 points (**Fig.S4a**) are 0.162 and 0.089, and the measured results are 0.143 and 0.119mm. For group A, the maximum relative

errors of calculated peak and average deformation are -31.04% and -26.04%.

The calculated peak deformation of B1 and B2/B3 are 0.213 and 0.160mm, and the measured results are 0.216 and 0.173mm; the calculated average value of 33 points (Fig.S4b) are 0.087 and 0.059mm, and the measured results are 0.157 and 0.103mm. The calculated peak deformation of B4 and B5/B6 are 0.346 and 0.314mm, and the measured results are 0.393 and 0.311mm; the calculated average value are 0.111 and 0.116mm, and the measured results are 0.186 and 0.153mm. For group B, the maximum relative errors of calculated peak and average deformation are -44.62% and -12.04%.

The effectiveness and accuracy of simulation model can be verified via the comparison between FEM and experiment results. In addition, as the main driving force, the effects of residual stress can be demonstrated via FEM simulation.



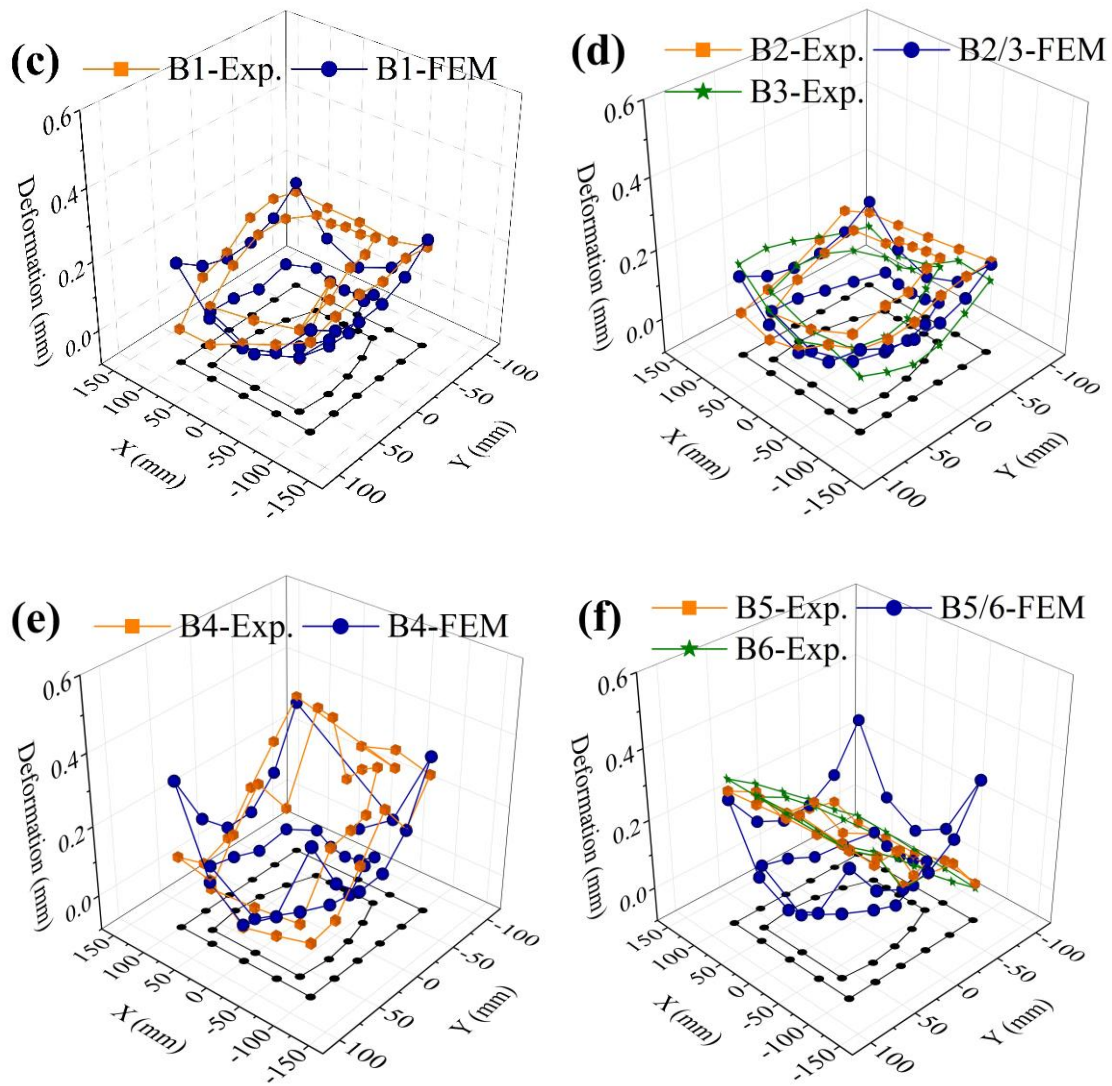


Fig.14 FEM and experiment results after 1st milling

5.2 Analysis of the deformation with time

In most cases, FE models can only calculate the machining deformation after 1st milling due to the uncertain evolution of residual stress during 96 hours natural aging, therefore, the variation of deformation with time can only be obtained by measurement tests rather than FEM simulations. Results shows that (**Fig.15** and **Fig.16**), compared with A1 (0.315mm), the peak deformations of A2 (0.264mm) and A3 (0.264mm) are reduced by 16.33% and 11.85%, and the average deformation of A2 (0.110mm) and A3 (0.127mm) is reduced by 23.10% and 10.86% ,

compared with A1 (0.143mm) at 24 hours after 1st milling.

Similarly, compared with B1 (0.216mm), the peak deformations of B2 (0.172mm) and B3 (0.174mm) are reduced by 20.33% and 19.69%. Compared with B1 (0.143mm), the average deformation of B2 (0.110mm) and B3 (0.127mm) are reduced by 25.02% and 43.74% at 24 hours after 1st milling. Compared with B4 (0.393mm), the peak deformations of B5 (0.320mm) and B6 (0.324mm) are reduced by 18.66% and 17.76%. Compared with B4 (0.186mm), the average deformation of B5 (0.149mm) and B6 (0.168mm) are reduced by 19.76% and 9.64% at 24 hours after 1st milling.

Besides, **Fig.15(a)**, **Fig.15(d)**, and **Fig.15(g)** also indicates that the overall dimension continuously changes with the time during 24-312 hours after machining. The change is significant within 24-72 hours after machining, it preliminarily reaches a stable state after 72 or 96 hours, and there is no significant change during 96-312 hours.

Other specimens, such as A2, A3, B2, B3, B5, and B6 (**Fig.15**), also has the same changing trend, namely reach a stable state after 72 or 96 hours, which means the strain energy accumulated by residual stress has been released in 72 or 96 hours. In this situation, the 2nd milling will not cause obvious deformation.

According to the measurement results, the changes of the maximum deformation of A2, A3, B2, B3, B5 and B6 caused by the 2nd milling are only 0.027, 0.030, 0.027, 0.026, 0.038, and 0.022mm because of the energy release after 1st milling, and the dimensions do not fluctuate evidently after the 2nd milling. In this study, the measured values at 96 hours after the final (2nd)

machining are taken as the final deformations. Thus, compared with A1, B1, and B4, the final maximum deformations of A2, B2, and B5 are reduced by 20.39%, 14.92%, and 3.80%, the average deformations are reduced by 1.60%, 15.39%, and 6.70%, and the dimension fluctuation in 96 hours after final milling are reduced by 74.69%, 68.56%, and 63.10%, respectively.

The deformation is determined by the total elastic strain energy Π_P of the part, which can be expressed as in Eq. (14) (Wang et al. [35] and Liu et al. [36]),

$$\Pi_P = U + W = \int_V \frac{1}{2} (\sigma_x \varepsilon_x + \sigma_y \varepsilon_y + \sigma_z \varepsilon_z + \tau_{xy} \gamma_{xy} + \tau_{xz} \gamma_{xz} + \tau_{yz} \gamma_{yz}) dV + W \quad (14)$$

where U is the strain energy density function, W is the work by external loads, σ_i and τ_{ij} are normal and shear stresses, ε_i and γ_{ij} are normal and shear strains, V is the volume of the body.

The external work W is zero in a free state.

When $\partial \Pi_P$ is close to 0, there is no sufficient energy for the part to deform. In this situation, the change rate of internal stress and strain is also 0, as a result, a relative stable state is achieved.

This explains the mechanism of deformation caused by stress release to a certain extent.

If 96 hours natural aging is replaced by TVSR, the final deformation can also be decreased. Compared with A1, B1, and B4, the final maximum deformations of A3, B3, and B6 are reduced by 23.51%, 24.16%, and 0.75%, the average deformations are reduced by 23.74%, 44.70%, and 21.30%, and the dimension fluctuation in 96 hours after final milling are reduced by 72.99%, 82.75%, and 78.94%, respectively. Results indicate that the TVSR process could significantly reduce strain energy and residual stress in the thin-walled part, and the deformation control effect is even better than 96 hours natural aging.

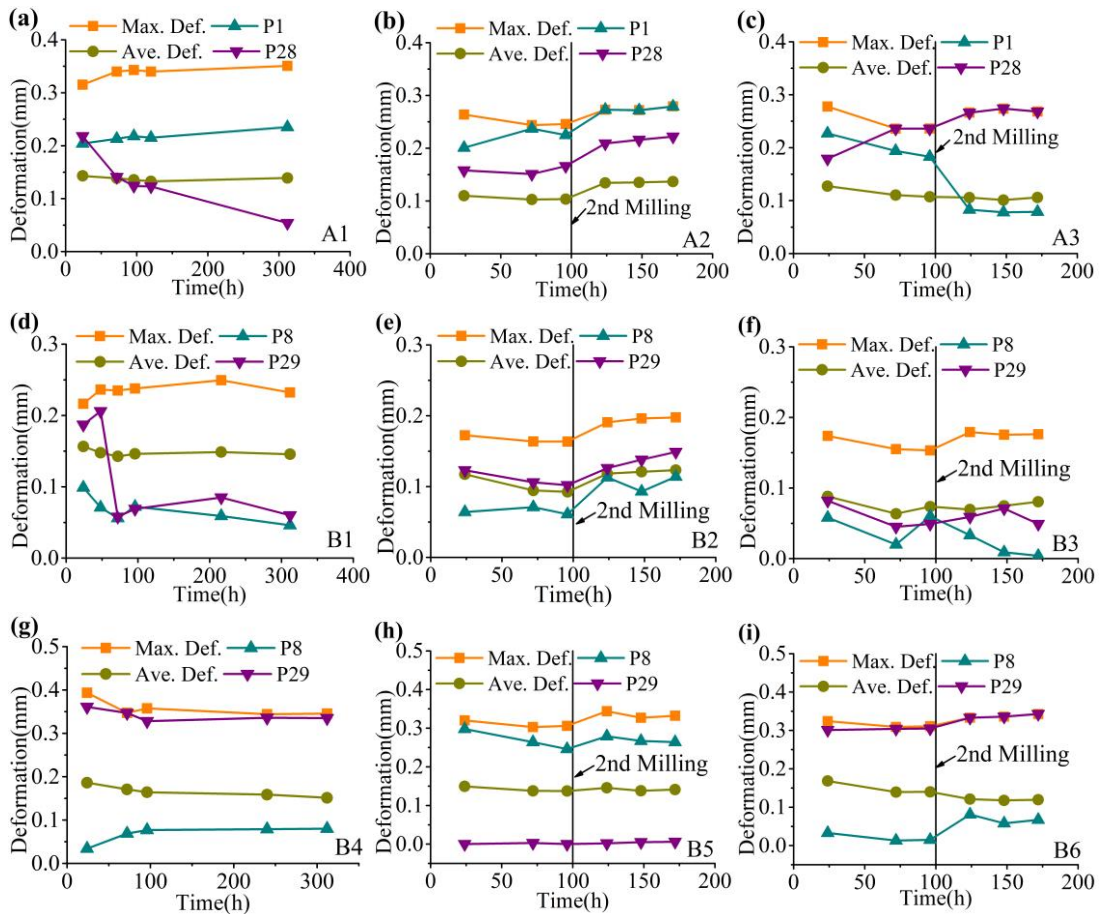
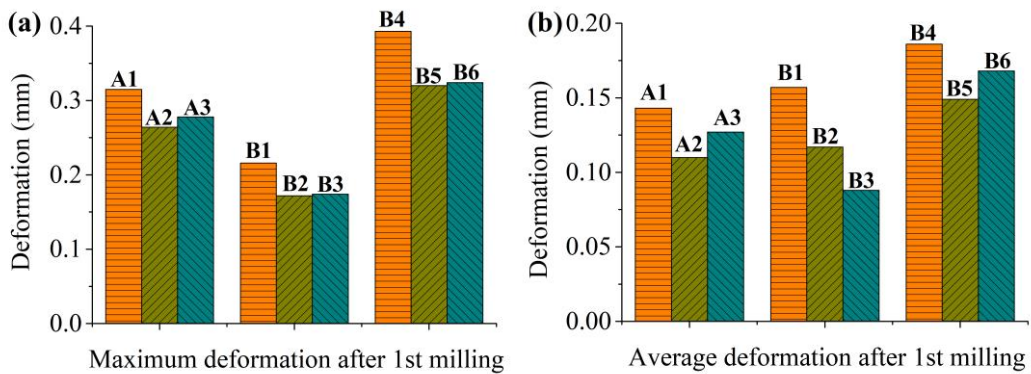


Fig.15 Measured variation of deformation with time of (a) A1, (b) A2, (c) A3, (d) B1, (e) B2, (f) B3, (g) B4, (h) B5, and (i) B6. (Except A1, B1 and B4, time after 100 hours represents the time after second milling + 100 hours)



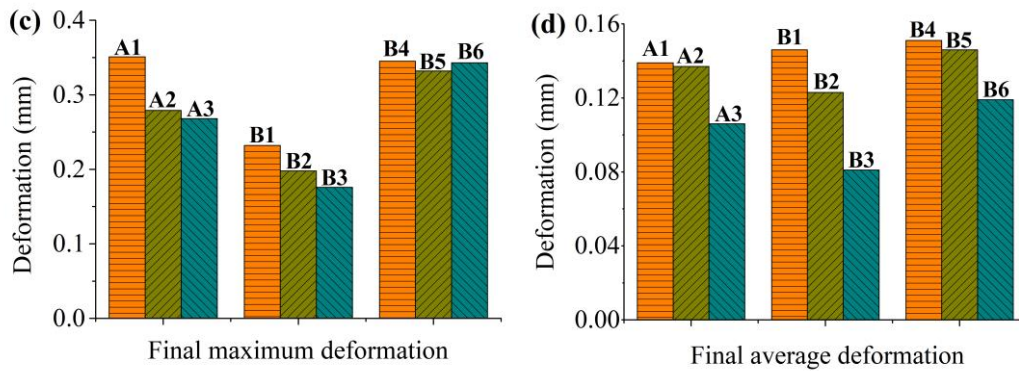


Fig.16 Deformation comparison: (a) Maximum deformation after 1st milling, (b) Average deformation after 1st milling, (c) Final maximum deformation, and (d) Final average deformation

5.3 Summary of deformation control method

In summary, the influences of equivalent bending stiffness and residual stress on the dimensional accuracy and stability in hundreds of hours after machining are investigated. It is found that the dimensions of the thin-walled parts continuously change with time after machining, and it preliminarily reaches a stable state after 72 or 96 hours with the release and rebalance of residual stress. This process can be accelerated using TVSR process for 5.7 hours. Compared with the original part (Process 1), the final deformation and dimension fluctuation are evidently decreased using Process 2 and 3 in this study.

At present, materials are usually reserved as the machining allowance in the position that is easy to be out of tolerance. However, according to the theory model of machining deformation, bending stiffness of the workpiece directly determines the magnitude of deformation. The machining deformation and dimension fluctuation will be further controlled if the allowance can enhance the bending stiffness.

According to the experiment and simulation results of this study, a machining deformation

control method based on topological optimization and stress relief process can be proposed, which has been proved to be effective in the machining of 7075 aluminum alloy and Ti6Al4V titanium alloy. The steps can be summarized as follows:

Step1: Designing the stiffening ribs as the machining allowance using FEM topological optimization;

Step2: Determining the intermediate workpiece according to topological optimization results;

Step3: Machining the intermediate workpiece in rough machining process;

Step4: Removing the fixture, and placing the workpiece statically in a free state for 96 hours or conducting TVSR process for 5.7 hours;

Step5: Machining the reserved stiffening ribs in the finish machining.

The proposed method could effectively decrease machining deformation and improve machining accuracy of monolithic thin-walled parts without changing process device and parameters. The experiment and simulation data as well as the proposed method can offer a theoretical foundation and data support for technicians to control deformation of the thin-walled parts.

6. Conclusions

In order to study the influence of equivalent bending stiffness and TVSR process on the dimensional stability of the monolithic thin-walled parts, nine typical parts in three groups with two materials (7075 aluminum alloy for A1~A3 and B1~B3, and Ti6Al4V titanium alloy for

B4~B6) are machined and treated with different processes. Topology optimization technique is used to optimize the structure of parts to enhance the bending stiffness. Corresponding FEM simulations are carried out to further investigate the generation mechanism. The deformations in hundreds of hours after machining are measured using coordinate measuring machine, and the deformation changes of the parts are obtained and analyzed. Finally, a machining deformation control method for thin-walled parts is proposed. Analyze the experimental results and get the following conclusions:

(1) The reserved stiffening ribs obtained by topological optimization can evidently enhance the bending stiffness. With the reserved stiffening ribs, the reduction rate of the maximum and average deformation at 24 hours after machining reach 20.33% and 43.74% for 7075 aluminium alloy parts, and those for Ti6Al4V parts reach 18.66% and 19.76%, respectively.

(2) The overall dimension of both 7075 aluminium alloy and Ti6Al4V continuously changes with the time during 24-312 hours after machining. The change is significant within 24-72 hours, it preliminarily reaches a stable state after 72 or 96 hours, and there is no significant change during 96-312 hours.

(3) When the 2nd milling for removing the reserved stiffening ribs is performed after 96 hours natural aging, no obvious deformation occurs because of the release and rebalance of the residual stress.

(4) The final maximum deformations of A2, B2, and B5 are reduced by 20.39%, 14.92%, and 3.80% with the process flow “1st milling reserving the stiffening ribs->waiting 96 hours->

2nd milling removing the ribs”, respectively.

(5) The final maximum deformations of A3, B3, and B6 are reduced by 23.51%, 24.16%, and 0.75%, when “waiting for 96 hours” is replaced by TVSR process.

(6) A machining deformation control method is proposed based on topological optimization and stress relief process.

The proposed method could effectively decrease machining deformation and improve machining accuracy of monolithic thin-walled parts without changing process device and parameters. The experiment and simulation data as well as the proposed method can offer a theoretical foundation and data support for technicians to control deformation of the thin-walled parts.

Declarations

Funding: This work was supported by Aeronautical Science Foundation of China (2019ZE051002); National Defense Basic Scientific Research program of China (JCKY2018601C002); and Anhui Postdoctoral Research Funding “Study on internal residual stress measurement method and TVSR process for additive manufacturing high strength aluminum alloy”.

Conflicts of interest/Competing interests: We declare that we have no conflict of interest or competing interests.

Availability of data and material: The data and material supporting the results of this study

are included within the article, and the original data of experiment and simulation are available from the corresponding author on reasonable request for academic communication.

Code availability: Not applicable.

Authors' contributions: The authors declare that they are all participants in the work and none of them performed only administrative functions.

References

[1] Z.T. Tang, T. Yu, L.Q. Xu, Z. Liu (2013) Machining deformation prediction for frame components considering multifactor coupling effects. *The International Journal of Advanced Manufacturing Technology* 68: 187-196. <https://doi.org/10.1007/s00170-012-4718-7>

[2] S. Fu, P. Feng, Y. Ma, L. Wang (2020) Initial residual stress measurement based on piecewise calculation methods for predicting machining deformation of aeronautical monolithic components. *International Journal of Advanced Manufacturing Technology* 108: 2063-2078. <https://doi.org/10.1007/s00170-020-05493-6>

[3] X. Huang, J. Sun, J. Li (2015) Finite element simulation and experimental investigation on the residual stress-related monolithic component deformation. *The International Journal of Advanced Manufacturing Technology* 77: 1035-1041. <https://doi.org/10.1007/s00170-014-6533-9>

[4] X. Huang, J. Sun, J. Li (2015) Effect of Initial Residual Stress and Machining-Induced Residual Stress on the Deformation of Aluminium Alloy Plate. *Strojnicki Vestnik-journal of*

Mechanical Engineering 61: 131-137. <https://doi.org/10.5545/sv-jme.2014.1897>

[5] J. Li, S. Wang (2017) Distortion caused by residual stresses in machining aeronautical aluminum alloy parts: recent advances. The International Journal of Advanced Manufacturing Technology 89: 997-1012. <https://doi.org/10.1007/s00170-016-9066-6>

[6] S. Ren, X. Long, G. Meng (2018) Dynamics and stability of milling thin walled pocket structure. Journal of Sound and Vibration 429: 325-347. <https://doi.org/10.1016/j.jsv.2018.05.028>

[7] W. Li, L. Ma, M. Wan, J. Peng, B. Meng (2018) Modeling and simulation of machining distortion of pre-bent aluminum alloy plate. Journal of Materials Processing Technology 258: 189-199. <https://doi.org/10.1016/j.jmatprotec.2018.03.019>

[8] Y. Sun, S. Jiang (2018) Predictive modeling of chatter stability considering force-induced deformation effect in milling thin-walled parts. International Journal of Machine Tools & Manufacture 135: 38-52. <https://doi.org/10.1016/j.ijmachtools.2018.08.003>

[9] L. Wang, H. Si (2018) Machining deformation prediction of thin-walled workpieces in five-axis flank milling. The International Journal of Advanced Manufacturing Technology 97: 4179-4193. <https://doi.org/10.1007/s00170-018-2248-7>

[10] Z.B. Wang, J.F. Sun, L.B. Liu, R.Q. Wang, W.Y. Chen (2019) An analytical model to predict the machining deformation of frame parts caused by residual stress. Journal of Materials Processing Technology 274: 1-13. <https://doi.org/10.1016/j.jmatprotec.2019.116282>

[11] J.W. Ma, G.Z. He, Z. Liu, F.Z. Qin, S.Y. Chen, X.X. Zhao (2018) Instantaneous cutting-

amount planning for machining deformation homogenization based on position-dependent rigidity of thin-walled surface parts. *Journal of Manufacturing Processes* 34: 401–411.

<https://doi.org/10.1016/j.jmapro.2018.05.027>

[12] Z. Kou, Y. Wan, Z. Liu, Y. Cai, X. Liang (2015) Deformation control in micro-milling of thin-walled structures. *The International Journal of Advanced Manufacturing Technology* 81: 967-974. <https://doi.org/10.1007/s00170-015-7258-0>

[13] X. Hao, Y. Li, Y. Cheng, C. Liu, K. Xu, K. Tang (2020) A time-varying geometry modeling method for parts with deformation during machining process. *Journal of Manufacturing Systems* 55: 15-29. <https://doi.org/10.1016/j.jmsy.2020.02.002>

[14] O. Sigmund, K. Maute (2013) Topology optimization approaches. *Structural and Multidisciplinary Optimization* 48: 1031-1055. <https://doi.org/10.1007/s00158-013-0978-6>

[15] J.D. Deaton, R.V. Grandhi (2014) A survey of structural and multidisciplinary continuum topology optimization: Post 2000. *Structural & Multidisciplinary Optimization* 49: 1-38. <https://doi.org/10.1007/s00158-013-0956-z>

[16] J. Vanek, J.A.G. Galicia, B. Benes (2014) Clever Support: Efficient Support Structure Generation for Digital Fabrication. *Computer Graphics Forum* 33: 117-125. <https://doi.org/10.1111/cgf.12437>

[17] M. Langelaar (2016) Topology optimization of 3D self-supporting structures for additive manufacturing. *Additive manufacturing* 12: 60-70. <https://doi.org/10.1016/j.addma.2016.06.010>

[18] J. Liu, A.T. Gaynor, S. Chen, Z. Kang, K. Suresh, A. Takezawa, L. Li, J. Kato, J. Tang, C.C.L. Wang, L. Cheng, X. Liang, A.C. To (2018) Current and future trends in topology optimization for additive manufacturing. *Structural and Multidisciplinary Optimization* 57: 2457-2483. <https://doi.org/10.1007/s00158-018-1994-3>

[19] J. Zhu, W. Zhang, L. Xia (2016) Topology Optimization in Aircraft and Aerospace Structures Design. *Archives of Computational Methods in Engineering* 23: 595-622. <https://doi.org/10.1007/s11831-015-9151-2>

[20] X. Wang, S. Xu, S. Zhou, W. Xu, M. Leary, P.F.M. Choong, M. Qian, M. Brandt, Y.M. Xie (2016) Topological design and additive manufacturing of porous metals for bone scaffolds and orthopaedic implants: A review. *Biomaterials* 83: 127-141. <https://doi.org/10.1016/j.biomaterials.2016.01.012>

[21] J. Liu, Y. Ma (2016) A survey of manufacturing oriented topology optimization methods. *Advances in Engineering Software* 100: 161-175. <https://doi.org/10.1016/j.advengsoft.2016.07.017>

[22] P. Dong, S. Song, J. Zhang (2014) Analysis of residual stress relief mechanisms in post-weld heat treatment. *International Journal of Pressure Vessels & Piping* 122: 6-14. <https://doi.org/10.1016/j.ijpvp.2014.06.002>

[23] B.-p. Gu, Z.-d. Jin, D.-j. Kong, J.-t. Lai, Z.-s. Yang, L. Pan (2017) Reduction of pulsed-laser surface irradiation induced residual stress using ultrasonic vibration method. *International Journal of Advanced Manufacturing Technology* 88: 755-765. <https://doi.org/10.1007/s00170->

[016-8798-7](#)

[24] H.-J. Gao, Y.-D. Zhang, Q. Wu, J. Song (2017) Experimental Investigation on the Fatigue Life of Ti-6Al-4V Treated by Vibratory Stress Relief. *Metals* 7: 62-67.

<https://doi.org/10.3390/met7050158>

[25] G. Yan, A. Crivoi, Y. Sun, N. Maharjan, X. Song, F. Li, M.J. Tan (2018) An Arrhenius equation-based model to predict the residual stress relief of post weld heat treatment of Ti-6Al-4V plate. *Journal of Manufacturing Processes* 32: 763-772.

<https://doi.org/10.1016/j.jmapro.2018.04.004>

[26] S.-G. Chen, Y.-D. Zhang, Q. Wu, H.-J. Gao, D.-Y. Yan (2019) Residual Stress Relief for 2219 Aluminum Alloy Weldments: A Comparative Study on Three Stress Relief Methods. *Metals* 9: 419-428. <https://doi.org/10.3390/met9040419>

[27] Q. Wu, W.S. Miao, H.J. Gao, Y.D. Zhang, D.J. Xie, M. Yang (2021) Residual stress homogenization of SiCP/Al composites with thermal vibration coupling. *International Journal of Advanced Manufacturing Technology* 112: 1691-1703. <https://doi.org/10.1007/s00170-020-06458-5>

[28] M. Koc, J. Culp, T. Altan (2006) Prediction of residual stresses in quenched aluminum blocks and their reduction through cold working processes. *Journal of Materials Processing Technology* 174: 342-354. <https://doi.org/10.1016/j.jmatprotec.2006.02.007>

[29] P. Ran, T. Pirling, J. Zheng, J. Lin, C.M. Davies (2018) Quantification of thermal residual stresses relaxation in AA7xxx aluminium alloy through cold rolling. *Journal of*

Materials Processing Technology 264: 454-468.

<https://doi.org/10.1016/j.jmatprotec.2018.09.034>

[30] H. Gong, X. Sun, Y. Liu, Y. Wu, Y. Wang, Y. Sun (2020) Residual Stress Relief in 2219 Aluminium Alloy Ring Using Roll-Bending. Materials 13: 105-120.

<https://doi.org/10.3390/ma13010105>

[31] H. Gao, Y. Zhang, Q. Wu, B. Li (2018) Investigation on influences of initial residual stress on thin-walled part machining deformation based on a semi-analytical model. Journal of

Materials Processing Technology 262: 437-448.

<https://doi.org/10.1016/j.jmatprotec.2018.04.009>

[32] Z. Zhang, L. Li, Y. Yang, N. He, W. Zhao (2014) Machining distortion minimization for the manufacturing of aeronautical structure. The International Journal of Advanced Manufacturing Technology 73: 1765-1773. <https://doi.org/10.1007/s00170-014-5994-1>

[33] B. Li, H. Deng, D. Hui, Z. Hu, W. Zhang (2020) A semi-analytical model for predicting the machining deformation of thin-walled parts considering machining-induced and blank initial residual stress. The International Journal of Advanced Manufacturing Technology 110: 1-23. <https://doi.org/10.1007/s00170-020-05862-1>

[34] H. Gao, S. Wu, Q. Wu, B. Li, S. Mo (2020) Experimental and simulation investigation on thermal-vibratory stress relief process for 7075 aluminium alloy. Materials & design 195: 108954. <https://doi.org/10.1016/j.matdes.2020.108954>

[35] Z. Wang, J. Sun, W. Chen, L. Liu, R. Wang (2018) Machining Distortion of Titanium

Alloys Aero Engine Case Based on the Energy Principles. *Metals* 8: 464-482.

<https://doi.org/10.3390/met8060464>

[36] L. Liu, J. Sun, W. Chen, J. Zhang (2016) Finite element analysis of machining processes of turbine disk of Inconel 718 high-temperature wrought alloy based on the theorem of minimum potential energy. *International Journal of Advanced Manufacturing Technology* 88:

3357–3369. <https://doi.org/10.1007/s00170-016-9026-1>

Supporting information

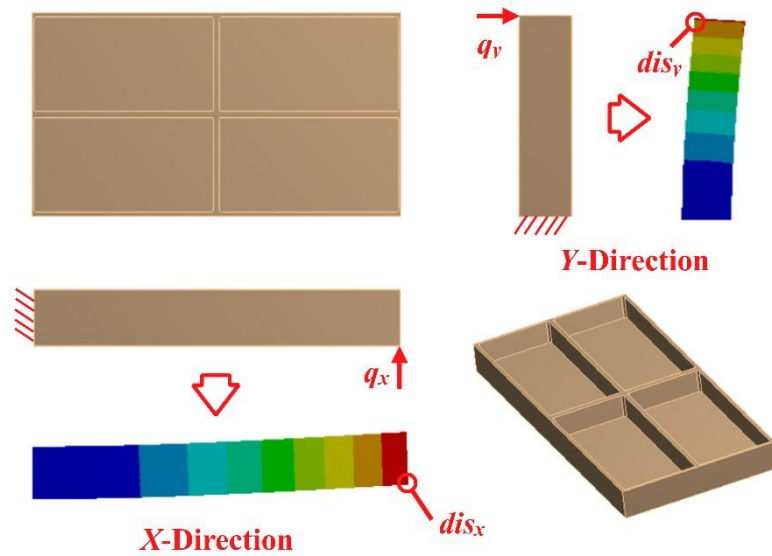


Fig.S1 Solution process of equivalent bending stiffness [31]

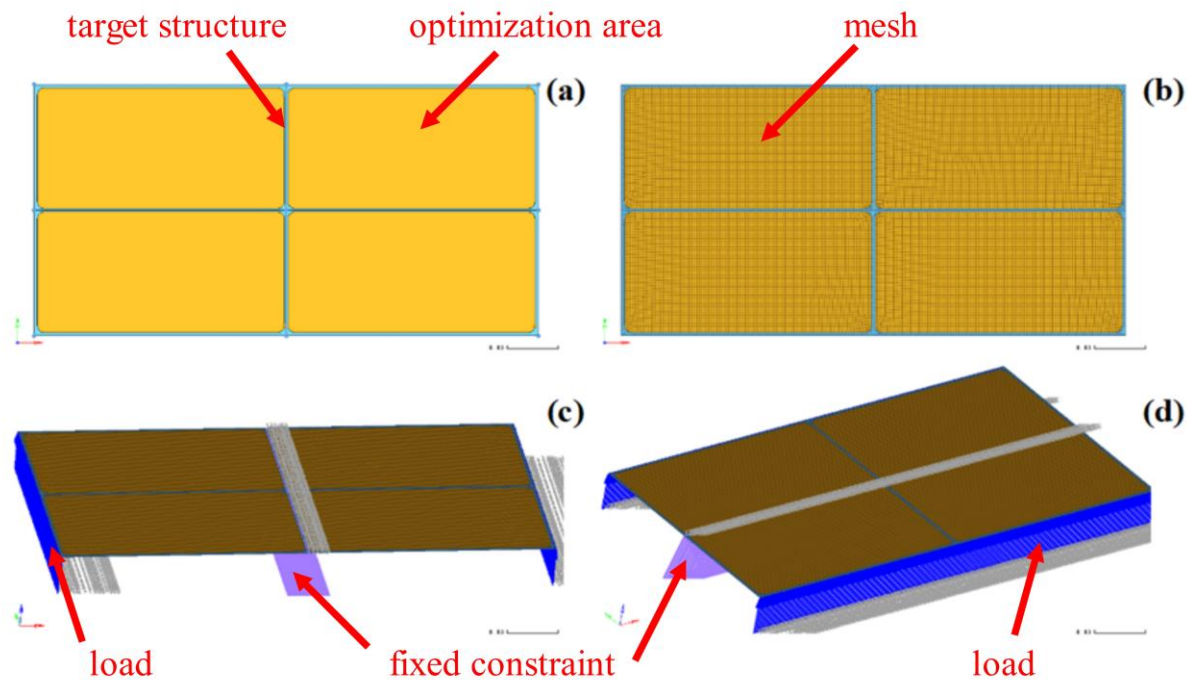


Fig.S2 FE model for topological optimization of A-type part: (a) two-dimensional section, (b) finite element mesh, (c) boundary condition of condition 1, and (d) boundary condition of condition 2.

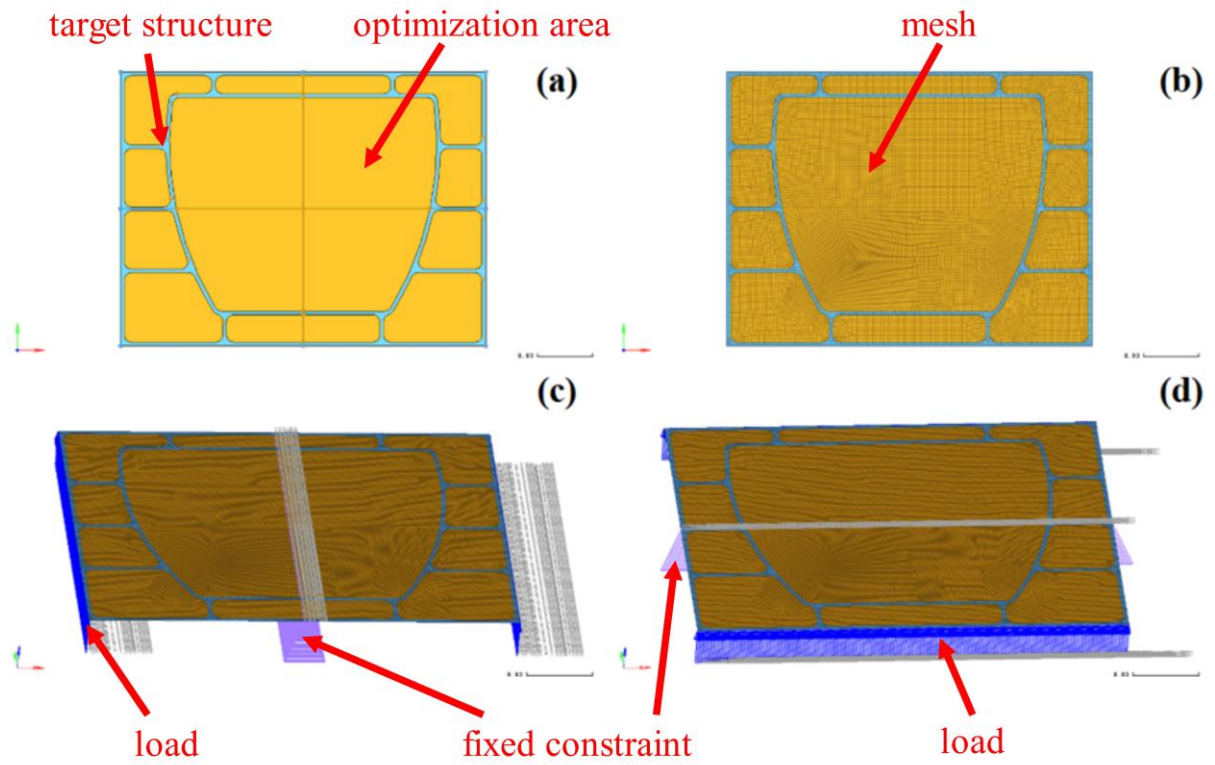


Fig.S3 FE model for topological optimization of B-type part: (a) two-dimensional section, (b) finite element mesh, (c) boundary condition of condition 1, and (d) boundary condition of condition 2.

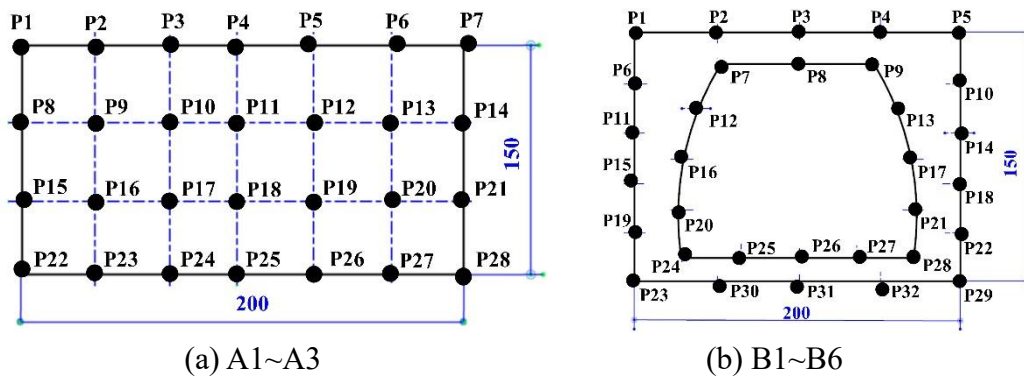


Fig.S4 Location and distribution of deformation measurement points

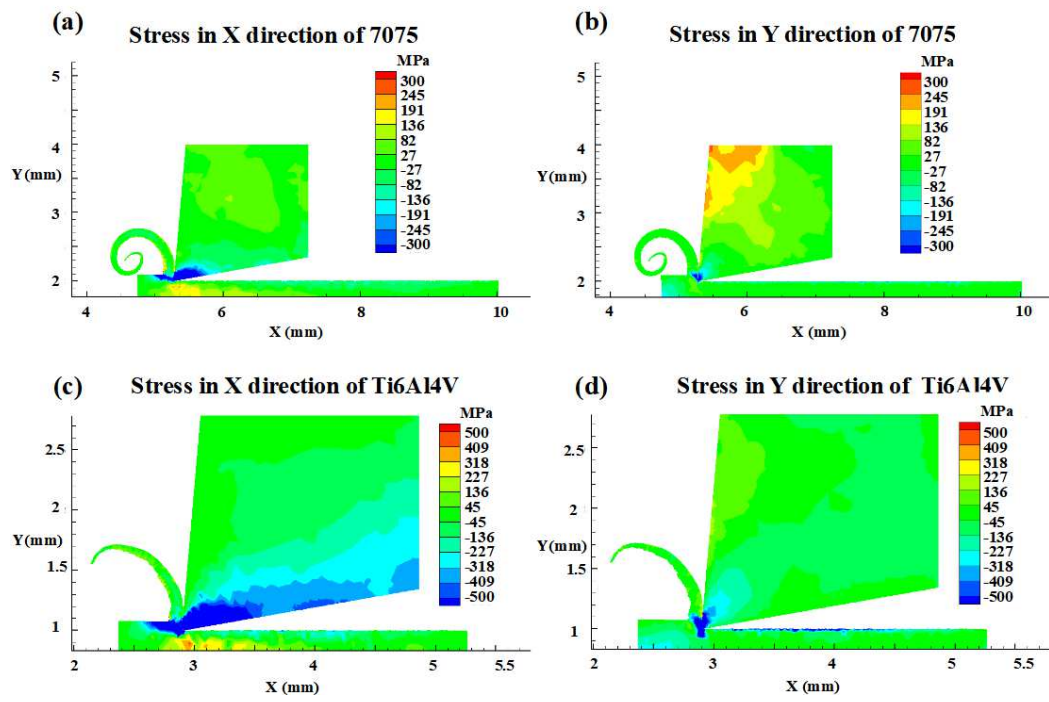


Fig.S5 FEM machining induced residual stress results.

Highlight:

- Topology optimization technique is used to optimize the structure of parts to reduce the machining deformation;
- The effects of natural aging and thermal and vibratory stress relief (TVSR) on the dimensional stability of thin-walled parts are studied;
- The machining experiments and corresponding FEM simulations are conducted, and deformations of thin-walled parts in hundreds of hours after machining are measured and analyzed;
- A machining deformation control method for thin-walled parts based on topological optimization and stress relief process is proposed;
- The final maximum deformations of three typical parts are reduced by 20.39%, 14.92%, and 3.80% with the proposed method.

Specific remarks

(1) What is your main contribution to the field?

Based on topological optimization and stress relief technology, a machining deformation control method for the monolithic thin-walled parts is proposed. Applying the new proposed method, the machining deformation can be decreased and the machining accuracy can be improved effectively.

(2) What is novel? In theory, in experimental techniques, or a combination of both?

The novel is reflected in the combination of theory and experimental techniques. The proposed method mentioned in (1) is the novel in theory, and the measures to reduce residual stress using thermal and vibratory stress relief is the improvement of process technology and experimental techniques.

(3) Does your paper have industrial applications? If yes, who are the likely user?

This method is in the experimental stage and has not been applied to industrial products.

Title page

Effects of residual stress and equivalent bending stiffness on
the dimensional stability of the thin-walled parts

Hanjun Gao^{a,b,c}, Xin Li^a, Qiong Wu^{a*}, Minghui Lin^a, Yidu Zhang^a

a. State Key Laboratory of Virtual Reality Technology and Systems, School of Mechanical Engineering and Automation, Beihang University, Beijing, 100191, PR China;

b. Anhui HengLi Additive Manufacturing Technology Co. LTD., Wuhu, 241200, PR China;

c. Anhui Chungu 3D Printing Institute of Intelligent Equipment
and Industrial Technology, Wuhu, 241220, PR China;

***Corresponding author:** Qiong Wu, wuqiong@buaa.edu.cn; Tel.: +86-10-8231-7756/+86-134-6661-7275;

Present address: New Main Building Room B313, Beijing University of Aeronautics and Astronautics, XueYuan Road No.37, HaiDian District, Beijing China. (Mail code in China: 100191)

E-mails:

Hanjun Gao: hjgao@buaa.edu.cn;

Xin Li: li_xin96@163.com;

Qiong Wu: wuqiong@buaa.edu.cn;

Minghui Lin: 1807039562@qq.com;

Yidu Zhang: ydzhang@buaa.edu.cn;

Figures

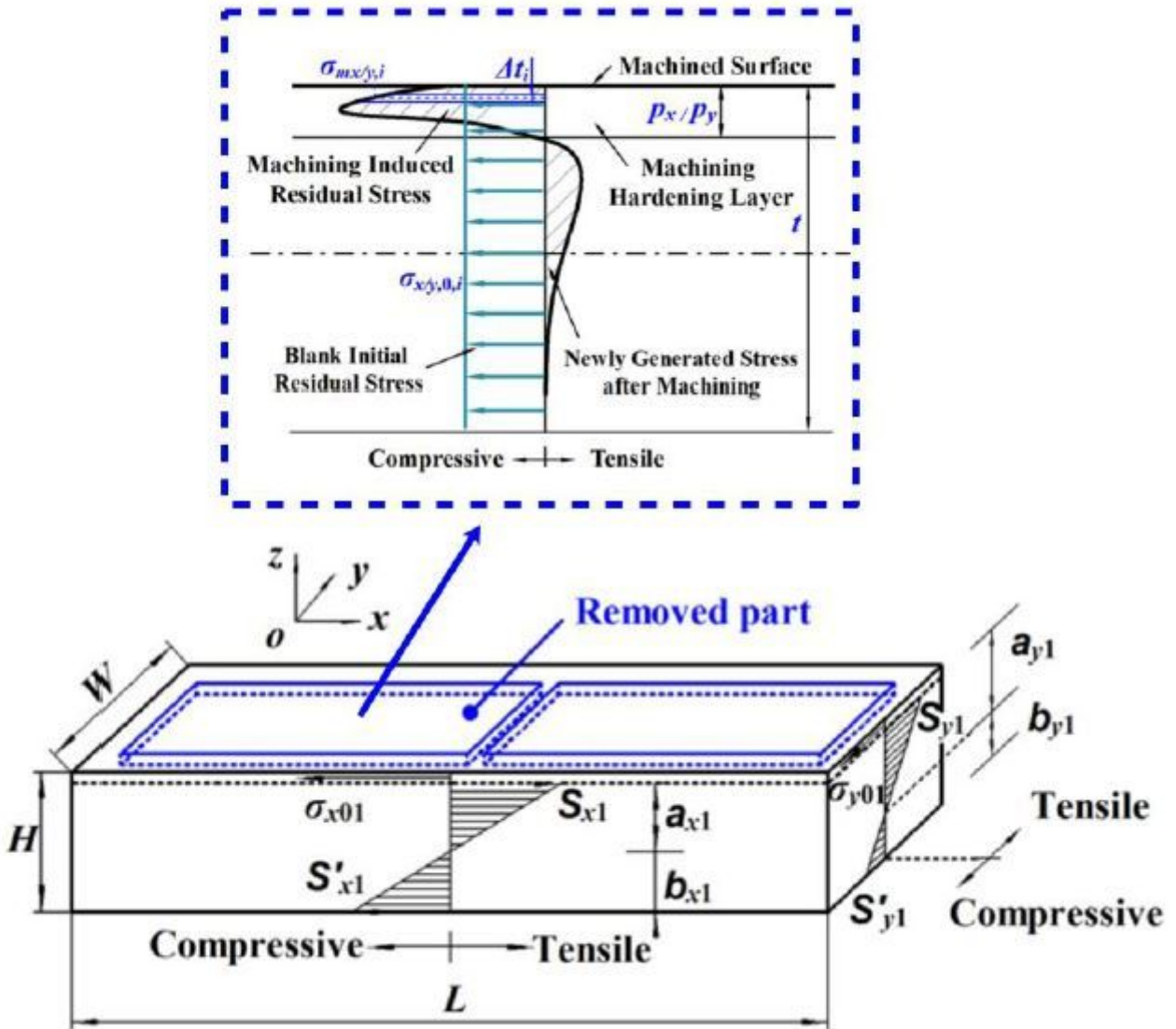


Figure 1

Deformation caused by blank initial and machining induced residual stress [33]

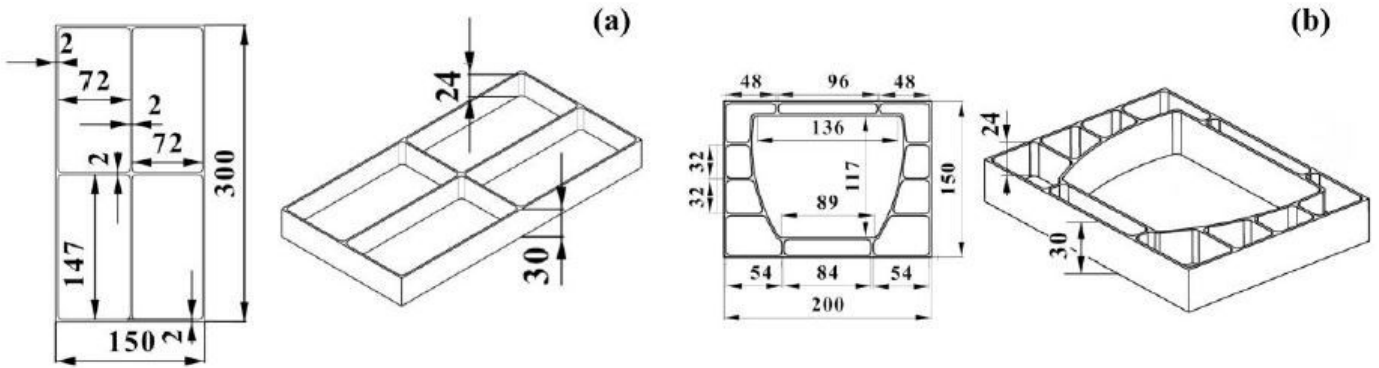


Figure 2

Size and shape sketch of two kinds thin wall parts(a)A-type part, and (b)B-type part

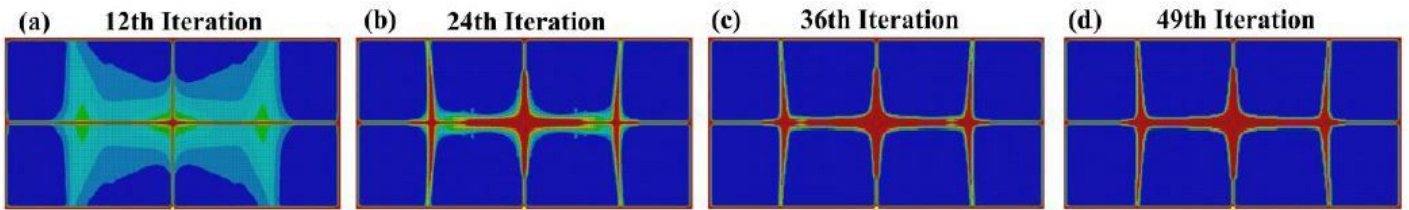


Figure 3

Topology optimization results of A-type parts after (a) 12th iteration, (b) 24th iteration, (c) 36th iteration, and (d) 49th iteration

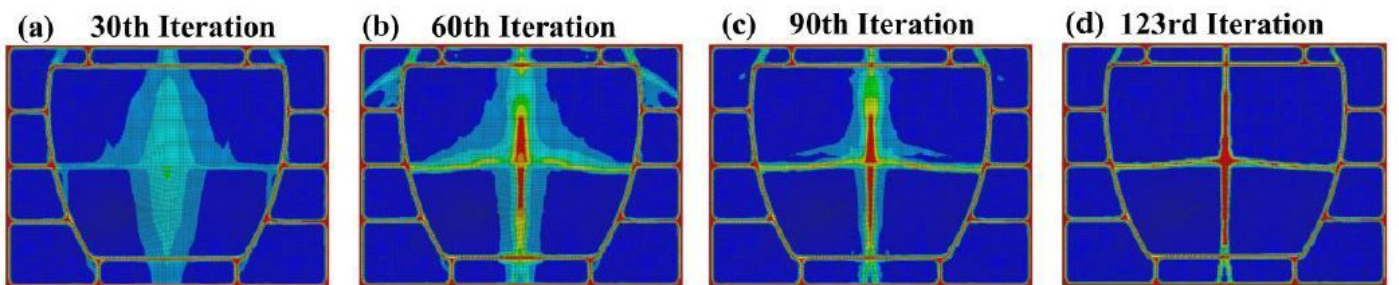


Figure 4

Topology optimization results of B-type parts after (a) 30th iteration, (b) 60th iteration, (c) 90th iteration, and (d) 123rd iteration

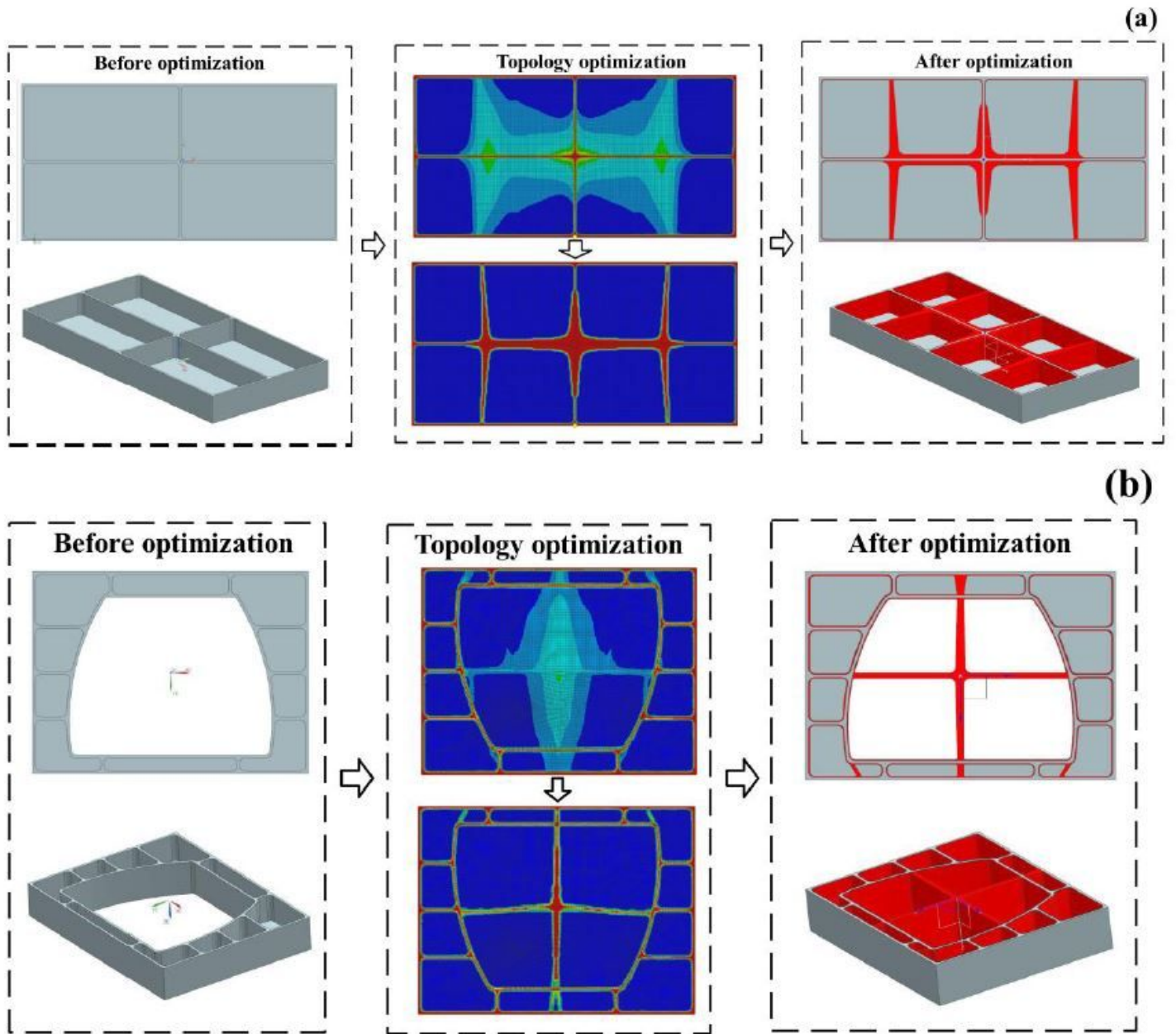


Figure 5

Design results of (a) Type A, (b) Type B

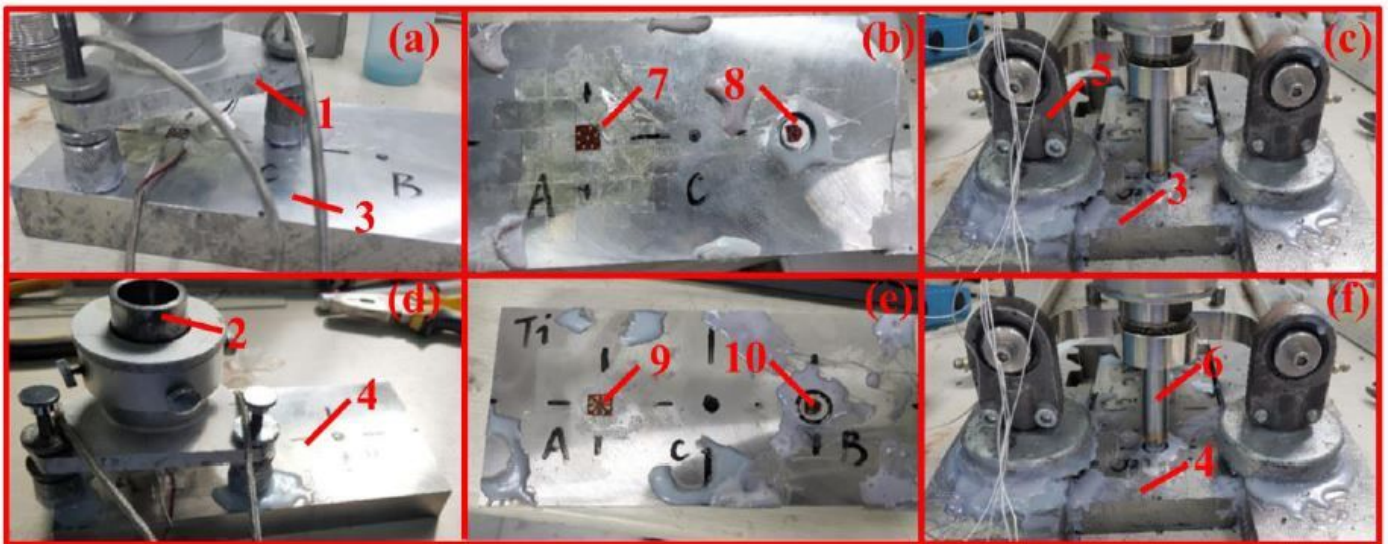


Figure 6

Residual stress measurement tests: (a) bland-hole method for 7075 aluminium alloy, (b) 7075 aluminium alloy specimen with measurement point, (c) ring-core method for 7075 aluminium alloy, (d) bland-hole method for Ti6Al4V, (e) Ti6Al4V specimen with measurement point, and (f) ring-core method for Ti6Al4V (1-Fixture of RS200, 2-SpinIde of RS200, 3-7075 aluminium alloy specimen, 4- Ti6Al4V specimen, 5-Fixture of RKV-18, 6-Spindle of RKV-18, 7-Blind-hold test point for 7075 aluminium alloy, 8-Ring-core test point for 7075 aluminium alloy, 9-Blind-hold test point for Ti6Al4V, and 10-Ring-core test point for Ti6Al4V)

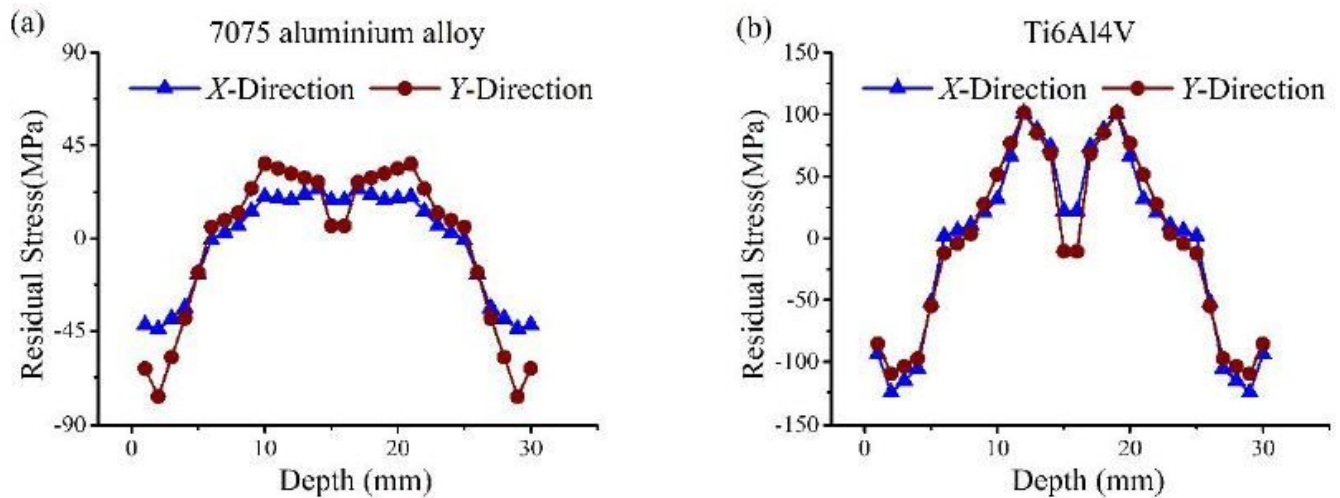
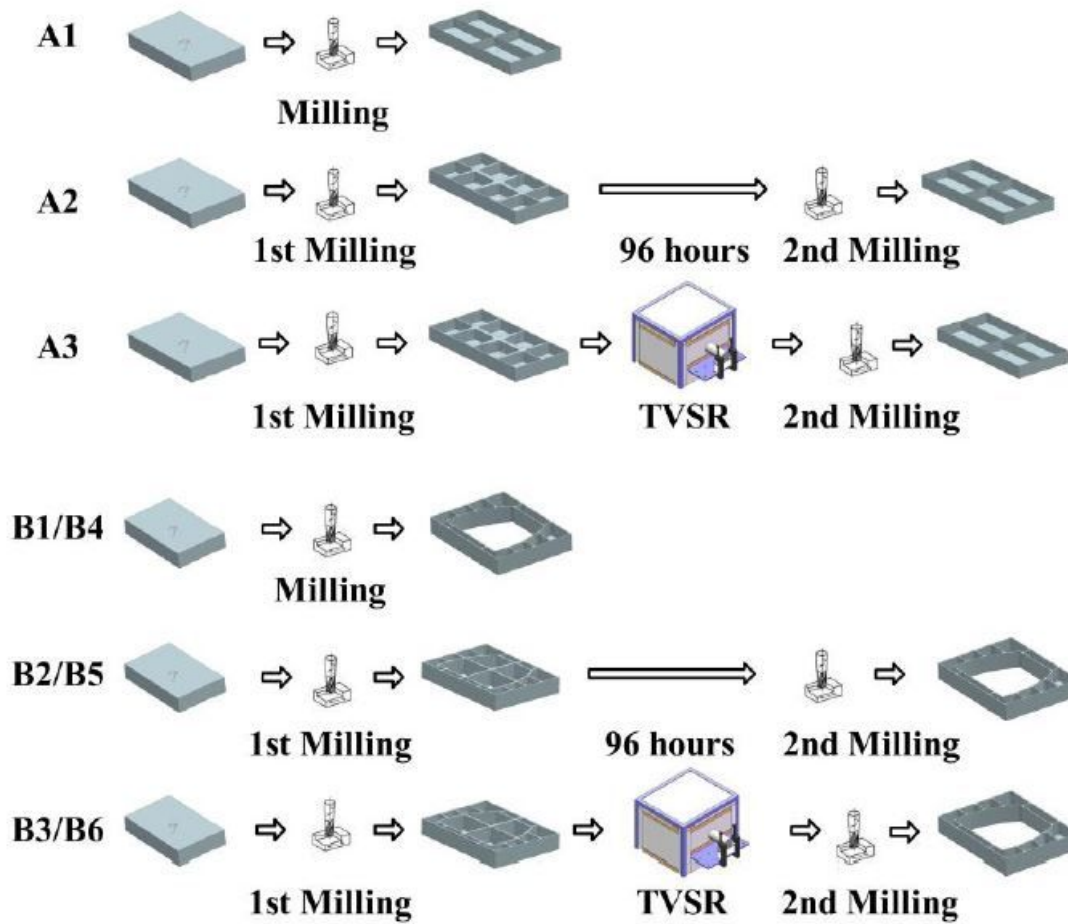


Figure 7

Residual stress profiles of (a) 7075 aluminium alloy and (b) Ti6Al4V



A1, A1, A3, B1, B2 and B3 are 7075 aluminium alloy, and B4, B5 and B6 are Ti6Al4V.

Figure 8

Process flows of the specimens

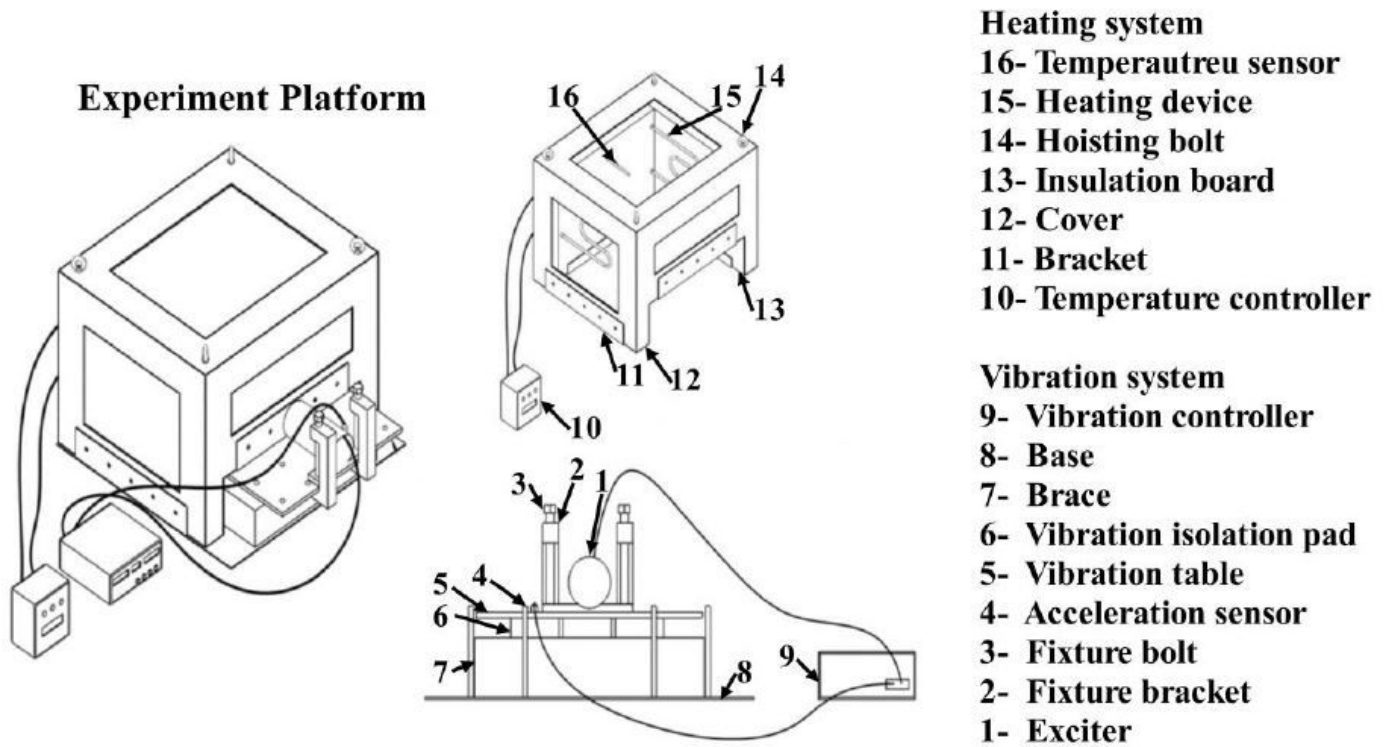
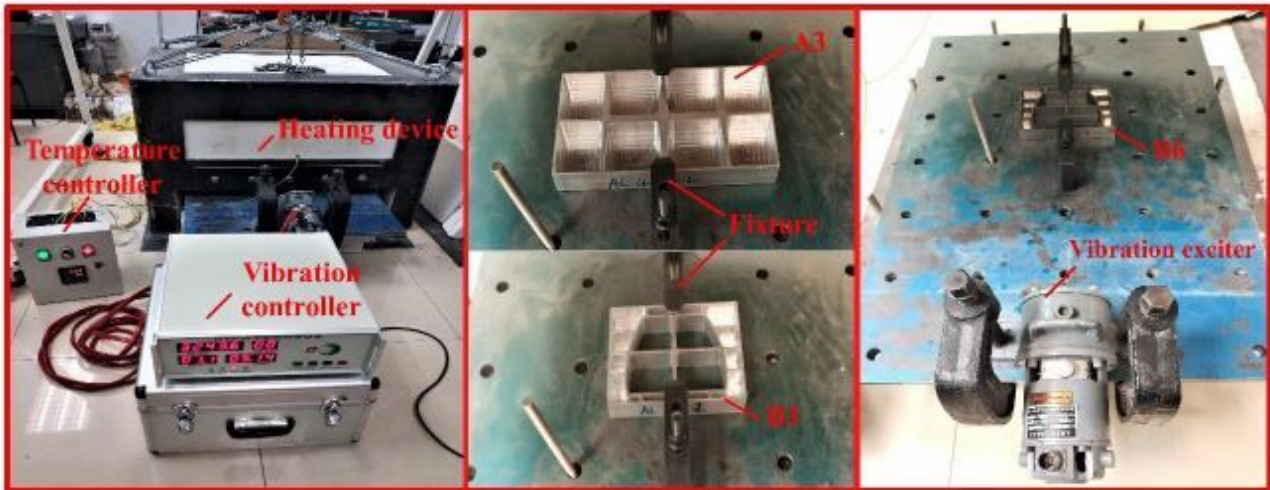


Figure 9

the schematic diagram of structural composition of TVSR [34]



(a)



(b)

Figure 10

NC machining and TVSR processing: (a) Part of the B-type parts on-site processing, and (b) TVSR of A-type and B-type parts

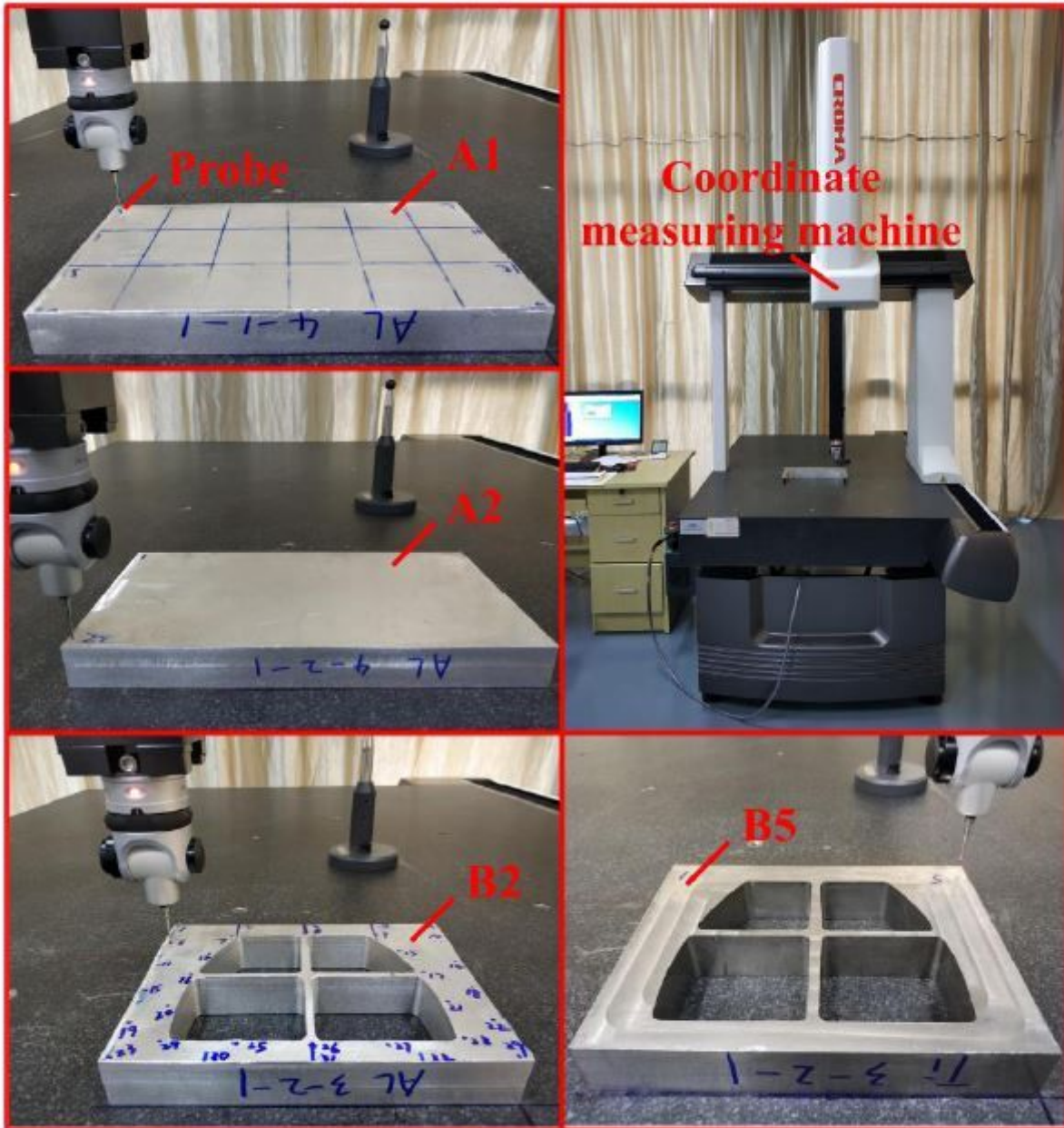


Figure 11

Deformation measurement experiment

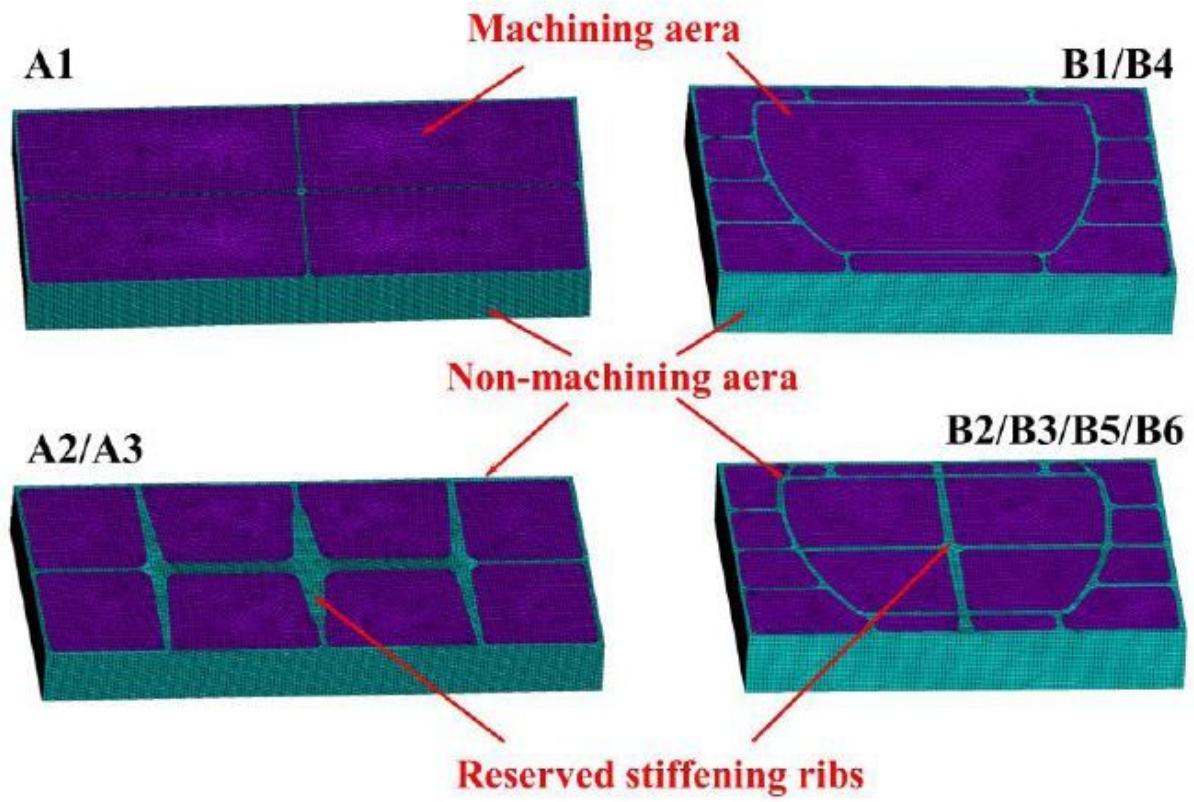


Figure 12

FE models of specimens

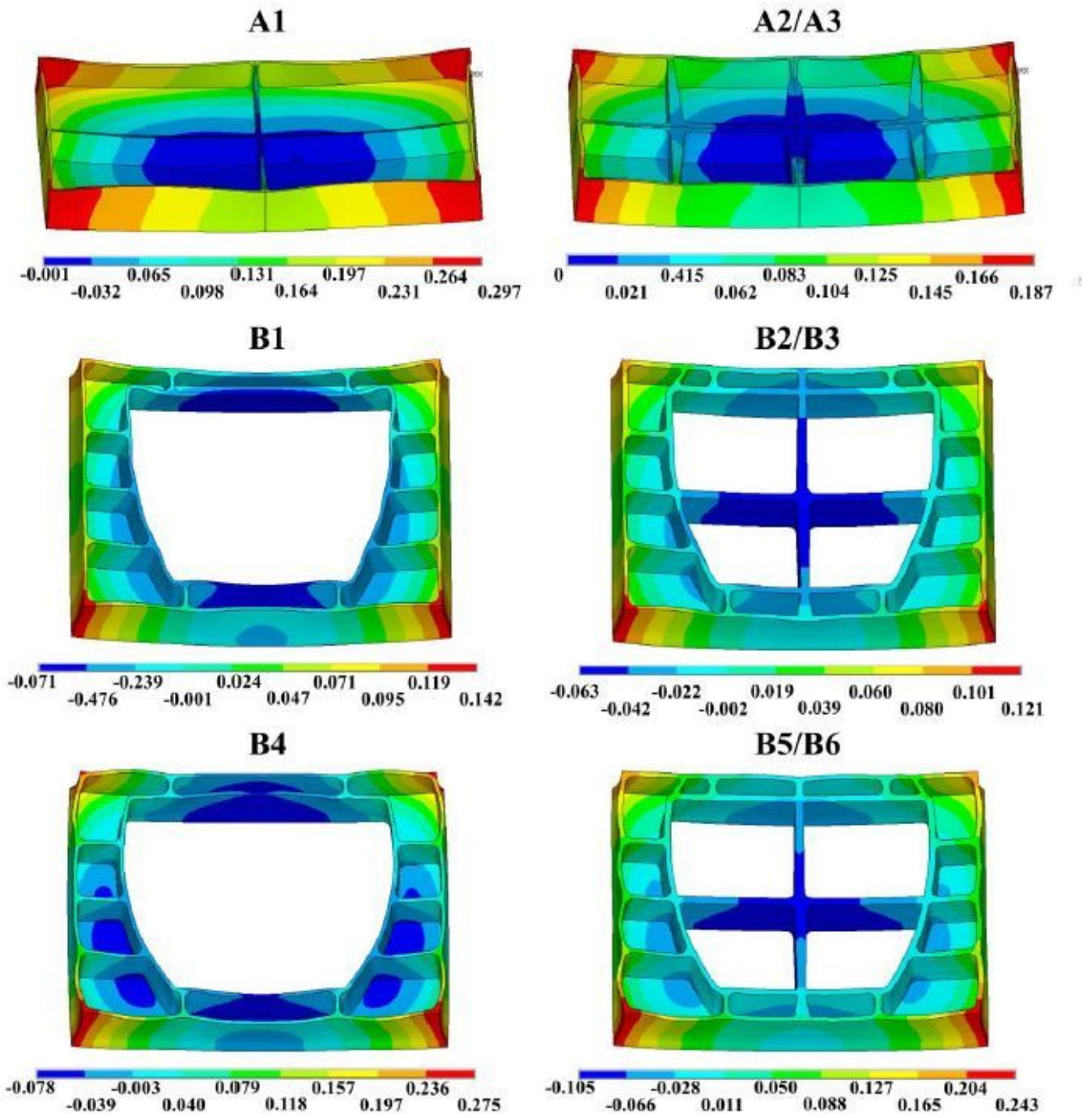


Figure 13

FEM deformation contours after 1st milling

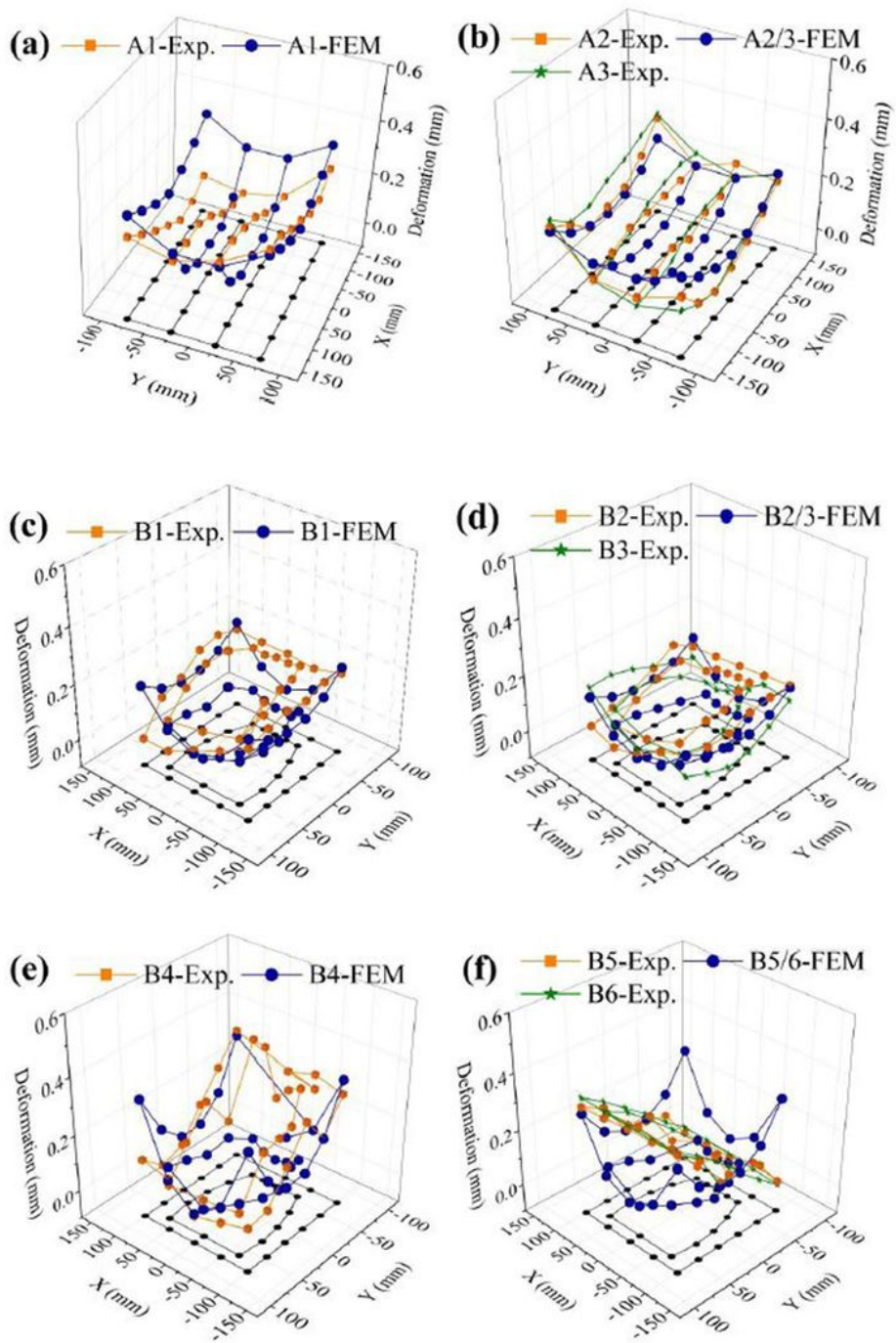


Figure 14

FEM and experiment results after 1st milling

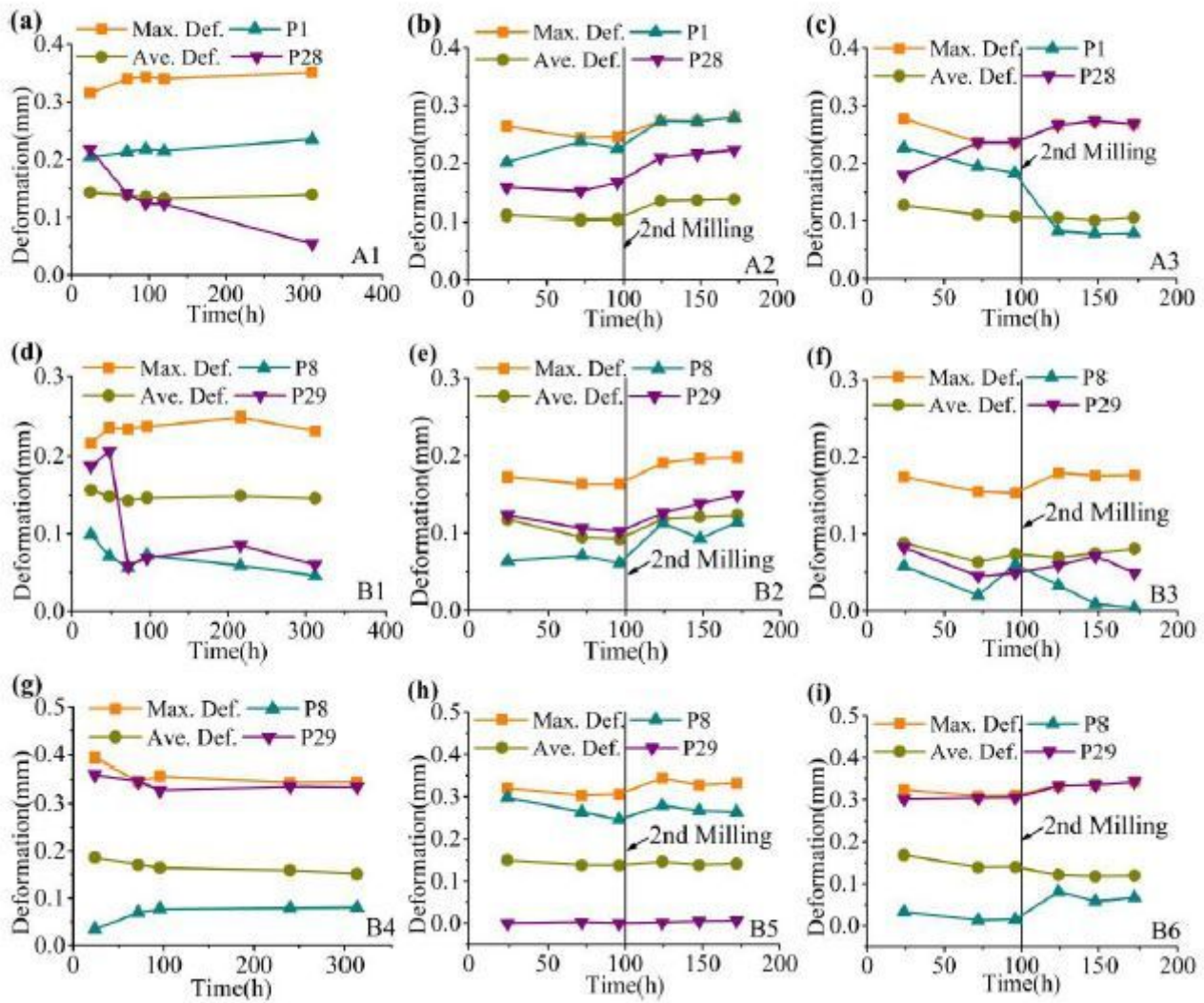


Figure 15

Measured variation of deformation with time of (a) A1, (b) A2, (c) A3, (d) B1, (e) B2, (f) B3, (g) B4, (h) B5, and (i) B6. (Except A1, B1 and B4, time after 100 hours represents the time after second milling + 100 hours)

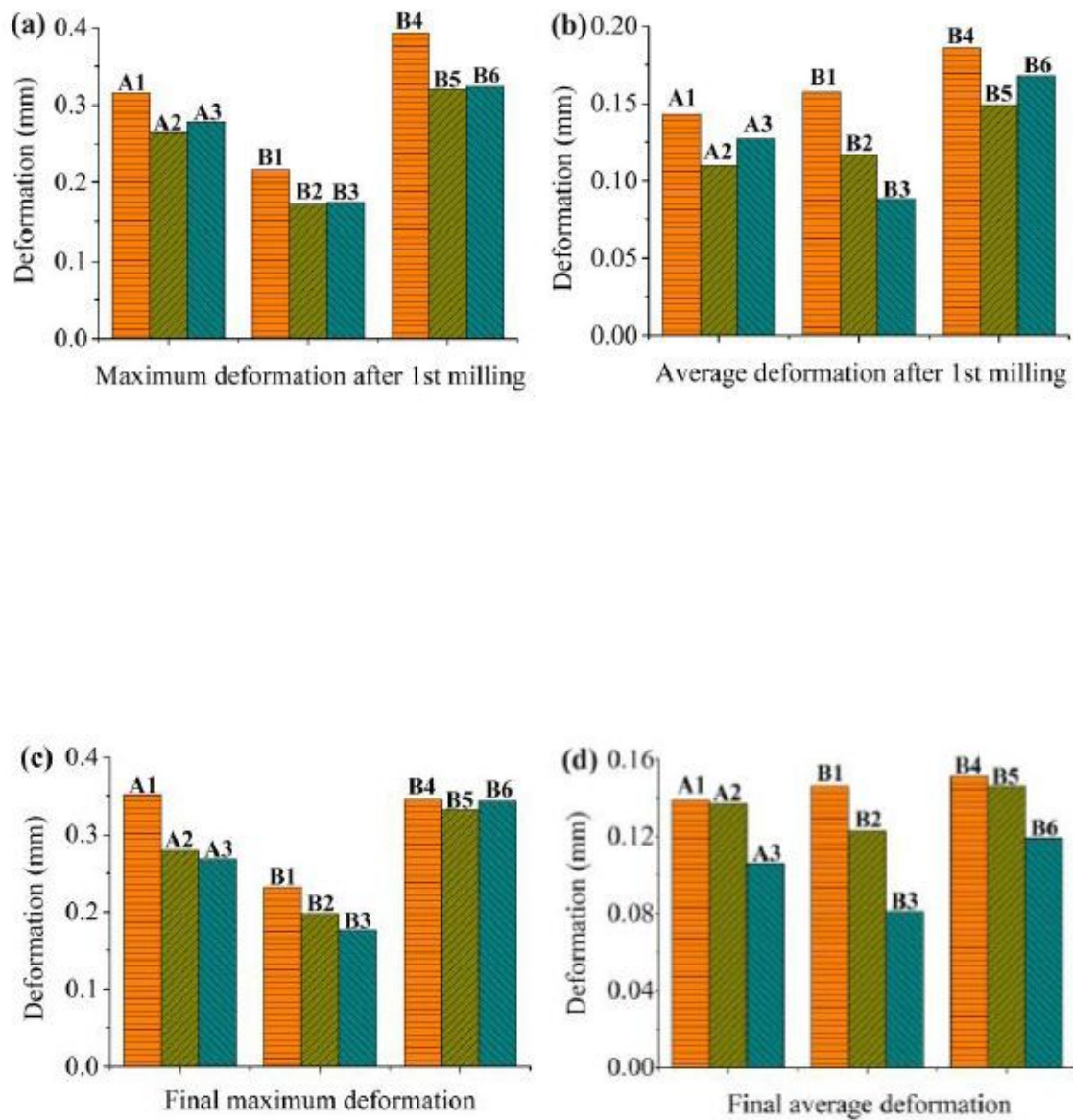


Figure 16

Deformation comparison: (a) Maximum deformation after 1st milling, (b) Average deformation after 1st milling, (c) Final maximum deformation, and (d) Final average deformation

Supplementary Files

This is a list of supplementary files associated with this preprint. Click to download.

- [GraphicalAbstract.jpg](#)
- [SupplementaryInformation.pdf](#)